
SHARED DIFFERENTIAL CLUSTERING ACROSS SINGLE-CELL RNA SEQUENCING DATASETS WITH THE HIERARCHICAL DIRICHLET PROCESS

Jinlu Liu

School of Mathematics
University of Edinburgh
Jinlu.Liu@ed.ac.uk

Sara Wade

School of Mathematics
University of Edinburgh
Sara.Wade@ed.ac.uk

Natalia Bochkina

School of Mathematics
University of Edinburgh
N.bochkina@ed.ac.uk

January 5, 2023

ABSTRACT

Single-cell RNA sequencing (scRNA-seq) is powerful technology that allows researchers to understand gene expression patterns at the single-cell level. However, analysing scRNA-seq data is challenging due to issues and biases in data collection. In this work, we construct an integrated Bayesian model that simultaneously addresses normalization, imputation and batch effects and also nonparametrically clusters cells into groups across multiple datasets. A Gibbs sampler based on a finite-dimensional approximation of the HDP is developed for posterior inference.

Keywords Clustering · Hierarchical Dirichlet process · Log-fold change · Markov Chain Monte Carlo · Single-cell RNA sequencing

1 Introduction

Technological developments in the detection of genetic sequences, such as single-cell RNA-sequencing (scRNA-seq), have enabled scientists to measure gene counts on a single-cell level. Moreover, experiments routinely collect multiple scRNA-seq datasets across different conditions, e.g. experimental conditions, disease subtypes, etc. Based on scRNA-seq data, different cell subtypes, with unique gene expression patterns, can be identified and examined by employing clustering methods. In this work, we aim to extend clustering methods appropriately in order to identify cell subtypes and estimate their proportions across different conditions, as well as identify potential unique and/or rare patterns that may be present in only a subset of conditions. In addition, it is also important to identify marker genes for each cell subtype that distinguish between the patterns observed across clusters.

Our work is motivated by experimental data collected to study prenatal development of cells under conditions when the transcription factor, Pax6, is knocked out in mutant mice [Mi et al., 2013]. In this case, it is believed that Pax6 controls the expression of receptors that allow cells to respond correctly to signals from other cells during development [Cabellaro et al., 2014]. Thus, we are interested in identifying clusters of cells with unique patterns of gene expression and dispersion; examining how cell-subtype proportions change when knocking out this factor; investigating if there are unique patterns present only in the mutant mice; and identifying marker genes.

However, analysing single-cell RNA sequencing data can be challenging due to issues and biases in the data collection. Specifically, only a small fraction of the total RNA present can be recorded, and thus, the data are very sparse, with zero values representing either true zero counts or missing values, also called dropouts. In addition, the fraction of transcripts recovered, also called the capture efficiency, varies across cells, causing high variability in expression levels and dropout rates. Moreover, batch effects are often present across experimental conditions, e.g. the control and mutant group, leading to further variability in capture efficiencies.

There has been a large amount of research in the field of normalization of observed gene counts to account for drop-outs, over-dispersions and batch effects. Often, the data are simply log-transformed [e.g. Finak et al., 2015], after adding

an offset to avoid the log of zero, and normalized in order to apply standard statistical tools. More recent approaches account for the count nature of the data directly, for example, through a negative-binomial model which also allows for over-dispersion [Vallejos et al., 2015, Risso et al., 2018, Tang et al., 2020].

In order to cluster cells and identify cell subpopulations, most approaches first apply a global normalization to the data. In addition, many methods also require some form of dimension reduction, typically via principal component analysis (PCA) [Senabouth et al., 2017, Satija et al., 2015, Lin et al., 2017] or t-distributed stochastic neighbour embedding (t-SNE) [Qiu et al., 2017]. Subsequently, a variety of clustering methods have been employed, such as hierarchical clustering [Senabouth et al., 2017, Lin et al., 2017, Gassen et al., 2015, Kiselev et al., 2017], k-means [Zurauskiene and Yau, 2016, Yang et al., 2017], density-based methods [Ester et al., 1996, Jiang et al., 2016], or model-based clustering [de Souto et al., 2008, Ji and Ji, 2016]. For recent reviews of clustering methods for scRNA-seq data, we refer the reader to Kiselev et al. [2019] and Petegrosso et al. [2020].

However, separating the workflow into the steps of global normalization, dimension reduction and clustering can adversely affect the analysis, resulting in improper clustering and characterization of cell subtypes [Prabhakaran et al., 2016, Vallejos et al., 2017]. More recent proposals integrate normalization and clustering in a combined model-based framework; not only does this allow for simultaneous recovery of clusters, inference of cell subtypes and normalization of the data based on cells with similar expression patterns, but it also provides measures of uncertainty through the model-based approach. Proposals include 1) Prabhakaran et al. [2016] who employ a Dirichlet process (DP) mixture of log-normal distributions and demonstrate the superiority of their approach compared with global normalization followed by clustering; 2) Sun et al. [2018] and Duan et al. [2019] who consider a DP mixture of multinomial distributions; and 3) Wu and Luo [2019] who combine the nested-hierarchical DP [Rodriguez et al., 2008] with a zero-inflated Poisson-log-normal distribution to cluster both subjects and cells in a nested fashion.

In this direction, we construct a Bayesian model which integrates normalization and shared clustering across conditions. In particular, we build on the *bayNorm* model [Tang et al., 2020], which directly accounts for the count nature and overdispersion of the data through a negative-binomial model and addresses normalization and imputation through an empirical Bayes approach. We combine *bayNorm* with the hierarchical Dirichlet process [HDP, Teh et al., 2006], in order to nonparametrically cluster cells, identify cell subtypes and infer varying cell-subtype proportions across conditions. Moreover, cells are clustered based on both mean expression and dispersion. This allows us to directly account for the mean-variance relationship, which provides robust estimates, particularly for sparse data and/or small clusters [Eling et al., 2018].

An important aspect of clustering scRNA-seq data is the discovery and identification of genes that distinguish one cluster from the others, often referred to as *marker genes* [Petegrosso et al., 2020]. Most methods identify marker genes after clustering, by performing some statistical tests, e.g. Satija et al. [2015] identify marker genes by applying the Wilcoxon rank-sum test to the expression values and Guo et al. [2015] use a mixture of the rank-sum test and Welch’s t-test depending on the sample size. Motivated by Vallejos et al. [2016], we go beyond simple comparison of mean expression levels; specifically, marker genes that characterize differences between cell subpopulations are detected based on the log-fold change (LFC) of expression values and dispersions across subpopulations. Other methods identify marker genes simultaneously within the clustering process [e.g. Zeisell et al., 2015, Olsson et al., 2016, Zhang et al., 2018].

In summary, we develop an integrated Bayesian model (Section 2) that simultaneously normalizes the data, clusters cells across conditions and infers cell subtypes with unique mean expression and dispersion patterns. A posterior inference scheme, as well as marker gene detection and posterior predictive checks are developed and described in Section 3. The effectiveness and robustness of the proposed model and probabilistic tools for detection of marker genes are demonstrated on simulated datasets in Section 4, and results on the motivating experimental data are presented in Section 5.

The experimental scRNA-seq datasets [Manuel et al., 2022] involved in this paper were collected and prepared by Dr. K. B. and the research group lead by Prof. D. Price and Prof. J. Mason at the Centre for Brain Discovery Science, University of Edinburgh. The study aims to shed light on the importance of the transcription factor PAX6 in the development and fates of embryonic cells. The scRNA-seq data was collected at day E13.5 from mouse embryos under control (HET) and mutant (HOM) conditions in which PAX6 has been deleted. Standard pre-processing for scRNA-seq is carried out to remove non-informative genes and cells from the raw datasets to improve model performance and avoid misinterpretation; pre-processing details are included in Web Appendix C, this involves selecting cells and genes based on Quality Control metrics [Stuart et al., 2019]. After pre-processing, the HET and HOM datasets contain $d_{C_2} = 5,282$ cells, respectively, both with $G = 2,529$ genes. The proposed Norm-HDP model is employed to identify cell subtypes, investigate how cell-subtype proportions change when PAX6 is knocked out, and explore if there are unique patterns when PAX6 is not present. The application of Norm-HDP model could be extended to any scRNA-seq datasets with equal number of genes per dataset.

2 The Model

To introduce notation, we observe scRNA-seq data in multiple conditions over the same genes, and the raw RNA counts for each condition d are collected in the matrix \mathbf{Y}_d for $d = 1, \dots, D$. Each \mathbf{Y}_d has elements $y_{c,g,d}$, with rows representing cells $c = 1, \dots, C_d$ and columns representing genes $g = 1, \dots, G$. The number of genes G is common across the conditions, while the number of cells C_d is condition-specific. In this work, we build on *bayNorm* [Tang et al., 2020], an integrated modelling approach to address simultaneously normalisation (correcting for variability in capture efficiencies), imputation (accounting for drop-outs), and batch effects. Specifically, we assume a binomial likelihood for the observed raw counts, given the unobserved true latent counts, denoted by $y_{c,g,d}^0$, and the cell-specific capture efficiencies, denoted by $\beta_{c,d}$:

$$y_{c,g,d} \mid y_{c,g,d}^0, \beta_{c,d} \stackrel{\text{ind}}{\sim} \text{Bin}(y_{c,g,d}^0, \beta_{c,d}).$$

The binomial distribution is a simple model for the transcript capture in scRNA-seq data, assuming the the observed count is obtained through independent Bernoulli experiments determining whether each of the true transcripts is captured, with a constant cell-specific probability (or capture efficiency). The latent counts are modelled with a negative-binomial distribution:

$$y_{c,g,d}^0 \mid \mu_{c,g,d}, \phi_{c,g,d} \stackrel{\text{ind}}{\sim} \text{NB}(\mu_{c,g,d}, \phi_{c,g,d}), \quad (1)$$

with mean expression level $\mu_{c,g,d}$ and dispersion parameter $\phi_{c,g,d}$. The negative-binomial, which can be represented as a Poisson-gamma mixture, is required when modelling RNA counts to capture the burstiness and excess variability observed, compared with a Poisson model. The latent counts can be marginalized to obtain the model:

$$y_{c,g,d} \mid \mu_{c,g,d}, \phi_{c,g,d}, \beta_{c,d} \stackrel{\text{ind}}{\sim} \text{NB}(\mu_{c,g,d} \beta_{c,d}, \phi_{c,g,d}). \quad (2)$$

We remark that the potential identifiability issues are apparent in the marginalized model in eq. (2); specifically, if all capture efficiencies are multiplied by a common factor and all mean expressions are divided by that same factor, the model is unchanged. To mitigate this, informative priors are used (Section 2.2).

A key difference between our model and *bayNorm* is that we allow for cell-specific mean expression $\mu_{c,g,d}$ and dispersion $\phi_{c,g,d}$ in eq. (1). We assume that the expression levels and dispersion parameters are generated from unknown, data-specific distributions P_d for $d = 1, \dots, D$, which are modelled with a hierarchical Dirichlet process [HDP, Teh et al., 2006]:

$$(\mu_{c,d}, \phi_{c,d}) \mid P_d \stackrel{\text{ind}}{\sim} P_d, \quad P_d \mid P \stackrel{\text{iid}}{\sim} \text{DP}(\alpha P), \quad P \sim \text{DP}(\alpha_0 P_0),$$

where $\mu_{c,d} = (\mu_{c,1,d}, \dots, \mu_{c,G,d})^T \in \mathbb{R}_+^G$ and $\phi_{c,d} = (\phi_{c,1,d}, \dots, \phi_{c,G,d})^T \in \mathbb{R}_+^G$ collect the mean expression and dispersion parameters for the c -th cell in dataset d across all genes; $\alpha > 0$ and $\alpha_0 > 0$ are the concentration parameters and P_0 is the base measure of the HDP; and DP denotes the Dirichlet process [Ferguson, 1973] discussed below.

2.1 The Hierarchical Dirichlet Process

The HDP [Teh et al., 2006] defines a distribution over a set of exchangeable random probability measures and is a widely adopted nonparametric prior due to its large support, interpretable parameters, and tractability. Realisations of the HDP are discrete with probability one, and an explicit construction is provided by the stick-breaking representation:

$$P_d = \sum_{j=1}^{\infty} p_{j,d} \delta_{\theta_j^*},$$

with $\theta_j^* = (\mu_j^*, \phi_j^*)$ and $\theta_j^* \stackrel{\text{iid}}{\sim} P_0$ and

$$\begin{aligned} p_{j,d} &= v_{j,d} \prod_{j' < j} (1 - v_{j',d}), & v_{j,d} \mid (p_1, \dots, p_j) &\sim \text{Beta} \left(\alpha p_j, \alpha \left(1 - \sum_{j'=1}^j p_j \right) \right), \\ p_j &= v_j \prod_{j' < j} (1 - v_{j'}), & v_j &\sim \text{Beta}(1, \alpha_0). \end{aligned}$$

Notice that the probability measures P_d share a common set of atoms θ_j^* , representing different cell subtypes with unique expression levels μ_j^* and dispersion ϕ_j^* , but have cell-subtype proportions $p_{j,d}$ that differ across datasets. The

discrete nature will induce ties in the cell-specific values of $\theta_{c,d} = (\mu_{c,d}, \phi_{c,d})$ with positive probability, and thus a random clustering of the cells is obtained, where two cells belong to the same cluster if they share the same expression level μ_j^* and dispersion ϕ_j^* . Moreover, clusters can be shared across multiple datasets. In fact, the law of this random clustering can be analytically obtained and described by the hierarchical Chinese restaurant franchise [Teh et al., 2006]. The HDP avoids pre-specifying a finite number of cell subtypes and instead assumes the number of cell subtypes in any finite sample is data-driven and grows with the number of cells.

The HDP can also be constructed as the limit of a finite-dimensional HDP defined as

$$P_d^J = \sum_{j=1}^J p_{j,d}^J \delta_{\theta_j^*}, \quad (3)$$

with $\theta_j^* \stackrel{iid}{\sim} P_0$ and

$$\begin{aligned} (p_{1,d}^J, \dots, p_{J,d}^J) | (p_1^J, \dots, p_J^J) &\sim \text{Dir}(\alpha p_1^J, \dots, \alpha p_J^J), \\ (p_1^J, \dots, p_J^J) &\sim \text{Dir}\left(\frac{\alpha_0}{J}, \dots, \frac{\alpha_0}{J}\right). \end{aligned} \quad (4)$$

Here, J represents the truncation level of the finite-dimensional approximation. As shown in Teh et al. [2006] and from the results of Kingman [1975], it follows that $P_d^J \Rightarrow P_d$.

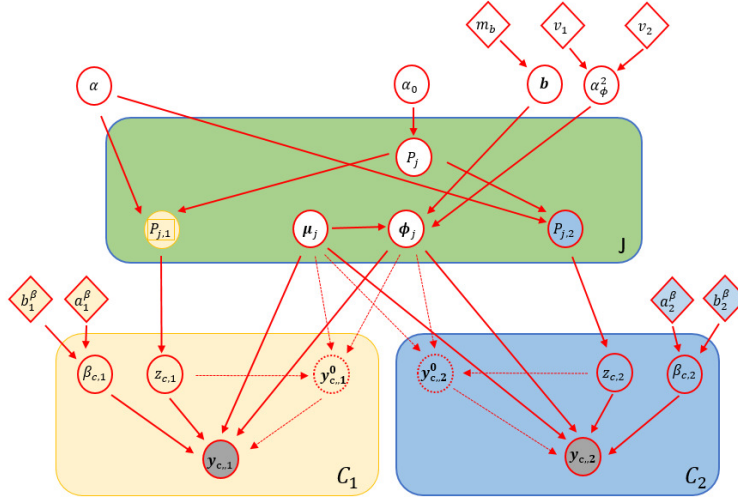


Figure 1: Graphical model of Norm-HDP with two datasets. Observed gene counts are shown in grey circles and estimated latent genes counts are shown in circles with dashed outlines. Shapes with white fills are for global parameters, and shapes with yellow and blue fills are specific to dataset 1 and 2, respectively. Circles denote parameters of interest, and diamonds denote fixed hyperparameters.

Figure 2 illustrates a simulation from the model in a simple setting with only one gene and a truncation at $J = 5$ cell subtypes. On the left, the mean and dispersion for each cell subtype is depicted, with size reflecting the cell-subtype proportion p_j of the base measure. The concentration parameter of the base measure is $\alpha_0 = 5$; as $\alpha_0 \rightarrow \infty$, the Dirichlet prior degenerates to a point mass at $(1/J, \dots, 1/J)$, while as $\alpha_0 \rightarrow 0$, the Dirichlet prior places all mass on the vertices of the simplex. Thus, large values of α_0 favor equal cell-subtype proportions in the base measure and small values of α_0 result in a large proportion for a single cell subtype. On the right of Figure 2, the cell-subtype proportions across two datasets are depicted for varying values of the HDP concentration parameter α , which controls the similarity of the data-specific cell-subtype proportions $p_{j,d}$ to the overall cell-subtype proportions p_j of the base measure. For a large value of $\alpha = 100$, the cell-subtype proportions for both datasets are similar to those of the base measure. As α decreases, the cell-subtype proportions become more distinct across datasets, and each dataset will contain only a single cell subtype in the limit as $\alpha \rightarrow 0$.

The finite-dimensional construction in eq. (3) provides good approximation of the HDP and is useful for approximate inference based on a finite truncation. A thorough study of the finite-dimensional Dirichlet approximation to the DP is given in Ishwaran and Zarepour [2002]. A nice feature is the exchangeability of the proportions p_j ; indeed, this is not the case for the truncated stick-breaking approximation [Ishwaran and James, 2001], which can suffer from an inflated

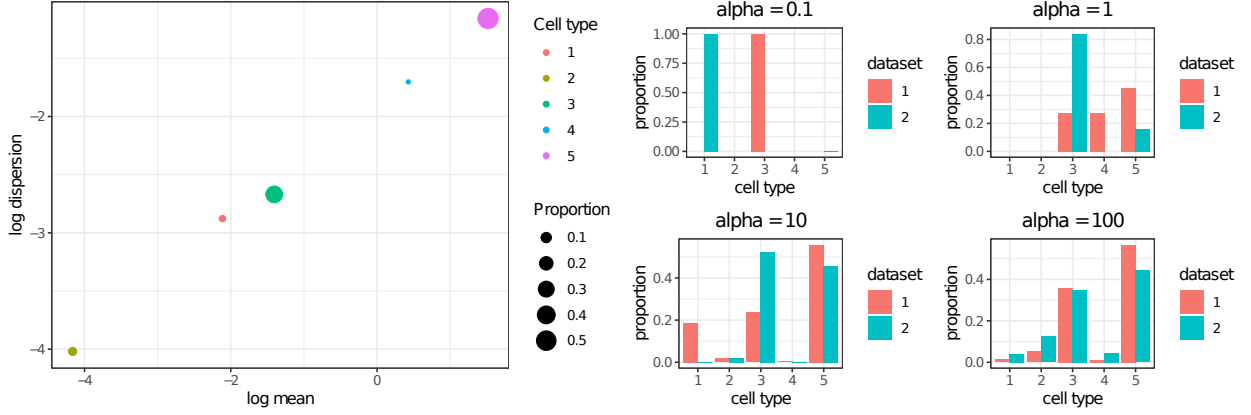


Figure 2: Simulation from the finite-dimensional HDP model, with $G = 1$ genes and $J = 5$ cell subtypes. Left: illustration of the mean and dispersion for each cell subtype, with size reflecting the cell-subtype proportion in the base measure. Right: cell-subtype proportions across two datasets for varying values of α . For a large value of $\alpha = 100$, the cell-subtype proportions for both datasets are similar to those of the base measure. As α decreases, the cell-subtype proportions become more distinct across datasets and degenerate to a single cell subtype per dataset as $\alpha \rightarrow 0$.

proportion p_J for the last atom if the truncation level is not sufficiently large. As shown in Miller and Harrison [2013], DP mixtures can lead to posterior inconsistency for the number of clusters, if the true number of clusters (in an infinite sample) is finite. However, the finite-dimensional Dirichlet approximations belong to the class of over-fitted or sparse mixtures, which have shown to be consistent for the true finite number of clusters [Rousseau and Mengersen, 2011]. However, this consistency requires correct specification of local likelihood [Miller and Dunson, 2015].

2.2 Prior Specification

The model is completed with prior specification for the other parameters, namely, P_0 of the HDP, the capture efficiencies $\beta_{c,d}$ and additional hyperpriors (e.g. for α, α_0). The base measure P_0 of the HDP determines the prior for the atoms θ_j^* which characterize the different cell subtypes. One main difference with other proposals in literature (e.g. Wu and Luo [2019]) is that our model allows both the mean expression and dispersion to be cell subtype-specific, i.e. the atoms are $\theta_j^* = (\mu_j^*, \phi_j^*)$. The motivations for this are two-fold; it allows 1) more general patterns to characterize differences between cell subpopulations and 2) inclusion of prior dependence between expression levels and dispersions to account for the mean-variance relationship. Recent studies have demonstrated the utility of exploring more general patterns, beyond focusing solely on differential expression [Korthauer et al., 2016]. For example, Vallejos et al. [2015] and Vallejos et al. [2016] develop tools to assess differential variability, which has led to novel biological insights [Martinez-Jimenez et al., 2017]. Moreover, a strong relationship is typically observed between mean expression and variability [Brennecke et al., 2013], suggesting that marker genes which are differentially expressed across subpopulations tend also to be differentially dispersed. Also, including prior dependence between expression levels and dispersions has shown to be important for sparse data and/or small sample sizes [Eling et al., 2018]; for our motivating dataset, we show that gene counts are truly sparse (Web Appendix C). Based on preliminary analysis of our motivating dataset (Web Appendix C), a parametric linear dependence appears sensible (in contrast to the nonlinear dependence in Eling et al. [2018]). Thus, the base measure is assumed to have the form:

$$P_0(d\mu^*) = \prod_{g=1}^G \log\text{-N}(\mu_g^* | 0, a_u^2), \quad P_0(d\phi^* | \mu^*) = \prod_{g=1}^G \log\text{-N}(\phi_g^* | b_0 + b_1 \log(\mu_g^*), a_\phi^2). \quad (5)$$

To enhance flexibility and assess robustness, we also consider a simple extension of eq. (5) based on a quadratic prior relationship between the mean-dispersion parameters.

For the hyperparameters of the mean-dispersion model $\mathbf{b} = (b_0, b_1)$ and a_ϕ^2 , we set $\mathbf{b} | a_\phi^2 \sim \text{N}(\mathbf{m}_b, a_\phi^2 \mathbf{V}_b)$ and $a_\phi^2 \sim \text{IG}(\nu_1, \nu_2)$, with default values of $\mathbf{m}_b = \mathbf{0}$, $\mathbf{V}_b = \mathbf{I}$, $\nu_1 = 2$, and $\nu_2 = 1$ [Eling et al., 2018]. We also consider an empirical prior by setting the values of \mathbf{m}_b , ν_1 and ν_2 based on the estimated linear relationship using the *bayNorm* estimates of the mean and dispersion parameters. The parameter a_u^2 is also set empirically based on the range of the mean estimates from *bayNorm*.

For the capture efficiencies, we assume $\beta_{c,d} \stackrel{iid}{\sim} \text{Beta}(a_d^\beta, b_d^\beta)$, where a_d^β and b_d^β are set empirically based on the mean and variance of the $\hat{\beta}_{c,d}$ obtained from *bayNorm*, which are estimated by combining cell-specific scaling factors with a global estimate of the mean capture efficiency for the experiment. This informative prior specification for the capture efficiencies helps to mitigate identifiability issues.

For HDP concentration parameters, we use the priors: $\alpha \sim \text{Gam}(1, 1)$ and $\alpha_0 \sim \text{Gam}(1, 1)$.

3 Posterior Inference

We focus on the finite-dimensional approximation of the HDP in eqs. (3)-(4) and introduce latent allocation variables $z_{c,d}$, where $z_{c,d} = j$ if $\theta_{c,d} = \theta_j^*$. Thus, the augmented model is:

$$\begin{aligned} y_{c,g,d} \mid z_{c,d} = j, \mu_{j,g}^*, \phi_{j,g}^*, \beta_{c,d} &\stackrel{ind}{\sim} \text{NB}(\mu_{j,g}^* \beta_{c,d}, \phi_{j,g}^*), \\ z_{c,d} \mid (p_{1,d}^J, \dots, p_{J,d}^J) &\stackrel{ind}{\sim} \text{Cat}(p_{1,d}^J, \dots, p_{J,d}^J), \\ (p_{1,d}^J, \dots, p_{J,d}^J) \mid (p_1^J, \dots, p_J^J) &\sim \text{Dir}(\alpha p_1^J, \dots, \alpha p_J^J), \\ (p_1^J, \dots, p_J^J) &\sim \text{Dir}\left(\frac{\alpha_0}{J}, \dots, \frac{\alpha_0}{J}\right), \\ \mu_{j,g}^* &\stackrel{iid}{\sim} \log\text{-N}(0, a_u^2), \quad \phi_{j,g}^* \mid \mu_{j,g}^* \stackrel{ind}{\sim} \log\text{-N}(b_0 + b_1 \log(\mu_{j,g}^*), a_\phi^2), \\ \beta_{c,d} &\stackrel{iid}{\sim} \text{Beta}(a_d^\beta, b_d^\beta), \end{aligned}$$

with hyperpriors: $\alpha \sim \text{Gam}(1, 1)$; $\alpha_0 \sim \text{Gam}(1, 1)$; and $(\mathbf{b}, \alpha_\phi^2) \sim \text{NIG}(\mathbf{m}_b, \mathbf{V}_b, \nu_1, \nu_2)$. A graphical representation of the proposed Norm-HDP model is shown in Figure 1.

A Markov chain Monte Carlo (MCMC) algorithm is developed for full posterior inference. The algorithm is a Gibbs sampler which produces asymptotically exact samples from the posterior by iteratively sampling the parameters in blocks. For the allocation variables ($z_{c,d}$), mean-dispersion hyperparameters $(\mathbf{b}, \alpha_\phi^2)$ and dataset-specific component probabilities ($\mathbf{p}_d = (p_{1,d}^J, \dots, p_{J,d}^J)$), the full conditional distributions correspond to standard distributions and can be sampled from directly. For the remaining variables, samples are obtained via adaptive Metropolis-Hastings [Griffin and Stephens, 2013]. We let T denote the total number of MCMC draws and use the superscript notation $z_{c,d}^{(t)}$ to denote the t -th sample. Full implementation details are provided in Web Appendix A. We note that each iteration of the Gibbs sampling algorithm has a computational complexity of $\mathcal{O}(\text{sum}(C)JG)$.

3.1 Latent Counts

To estimate the normalized count of gene g in cell c , we report the posterior mean of the latent count $y_{c,g,d}^0$, along with posterior summaries to characterize uncertainty. Following Tang et al. [2020], it can be shown the posterior of the latent count given the allocation variables, capture efficiencies and unique parameters has a shifted negative-binomial distribution:

$$y_{c,g,d}^0 = y_{c,g,d} + \zeta_{c,g,d},$$

where $\zeta_{c,g,d}$ represents the *lost* count, which has a negative-binomial distribution with mean $\mu_{z_{c,d},g}^* (1 - \beta_{c,d}) (y_{c,g,d} + \phi_{z_{c,d},g}^*) / (\mu_{z_{c,d},g}^* \beta_{c,d} + \phi_{z_{c,d},g}^*)$ and size $y_{c,g,d} + \phi_{z_{c,d},g}^*$. Thus, the posterior mean of the latent count given the allocation variables, capture efficiencies and unique parameters is given in Web Appendix A. We can also examine the full posterior of the latent counts and compute credible intervals by drawing values $y_{c,g,d}^0$ from the shifted negative-binomial distribution at each MCMC draw.

3.2 Clustering

To summarize the posterior of the allocation variables, we construct the posterior similarity matrix (PSM) to measure the similarity between individual cells, both within and across datasets. In particular, each element of the posterior similarity matrix, $\text{PSM}_{c,c'}$, represents the posterior probability that cells c and c' are clustered together, which is approximated by

$$\text{PSM}_{c,c'} \approx \frac{1}{T} \sum_{t=1}^K \mathbf{I}(z_c^{(t)} = z_{c'}^{(t)}).$$

Cells are ordered in blocks corresponding to the different datasets; thus, the diagonal blocks represent the posterior similarity matrix within each dataset and the off-diagonal blocks represent the posterior similarity matrix across datasets. Within each block, cells are sorted based on hierarchical clustering to improve visualization. Based on the posterior similarity matrix, we obtain a point estimate of the clustering structure by minimizing the posterior expected variation of information [Wade and Ghahramani, 2018].

3.3 Detecting Marker Genes

Motivated by Vallejos et al. [2016], probabilistic tools are developed based on the LFC to detect marker genes that distinguish between different cell types. Vallejos et al. [2016] focus on comparing two cell populations; thus, a simple extension is proposed which takes all clusters into consideration. Going beyond comparison of mean expression levels, we aim to detect marker genes both in terms of differential mean expression (DE) and differential dispersion (DD). For example, DD allows identification of genes whose expression may be less stable in one cell subtype.

We define two types of marker genes; *global* marker genes differ between at least two clusters, whereas *local* marker genes for a given cluster differ compared with all other clusters. Full derivations and computations of *global* and *local* marker genes are found in Web Appendix A. Figure 3 illustrates the hypothetical latent count density for two genes and four cell subtypes. Both genes are global markers, but the gene on the left is a local marker for cell-subtypes 3 and 4 only, while the gene on the right is not a local marker for any cell subtype.

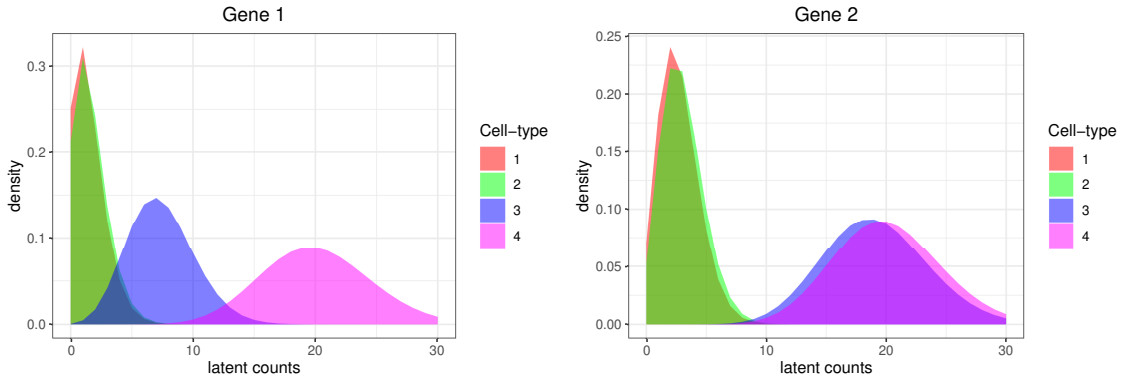


Figure 3: Density of hypothetical latent counts across four cell subtypes for two genes. Both genes are global marker genes, while the gene on the left is a local marker gene for cell-subtypes 3 and 4 and the gene on the right is *not* a local marker gene for any cell subtype.

3.4 Posterior Predictive Checks

Posterior predictive checks are used to assess the fit of the model together with the inferred parameters to the observed data. In particular, we generate replicated datasets from the posterior predictive distribution (approximated based on the MCMC draws) and compare key statistics between the observed and replicated data, such as the mean and standard deviation of the log counts (shifted by 1) and the dropout probabilities. Following Lewin et al. [2007] in the context of gene expression data, we employ mixed posterior predictive checks, where the posterior distribution is used to simulate a subset of parameters, the prior distribution is used to simulate the remaining variables, and checks are limited to observations with high allocation probabilities. In particular, we generate replicated datasets after first simulating dispersions (ϕ) from their log-normal prior given the posterior samples of \mathbf{b} , α_ϕ^2 and μ .

4 Simulation Study

We consider three simulated scenarios to examine different aspects of our model. In Simulation 1, data is simulated based on the proposed model, and we investigate the ability of the model to recover the true parameters and clustering. In Simulation 2, we study robustness of the model under misspecification of the true mean-variance relationship. In Simulation 3, we assume that only a fraction of genes distinguish between clusters to demonstrate the effectiveness of the proposed probabilistic tools for detecting global marker genes.

4.1 Simulation 1 and 2

In Simulation 1, we assume the true relationship between the mean-dispersion parameters is linear on the log-scale, while in Simulation 2, we assume it is non-linear and non-quadratic, but monotonically increasing on the log-scale (Web Appendix B.4). For both, we simulate data with $C_1 = 50$ cells in dataset 1 and $C_2 = 100$ cells in dataset 2, with $G = 50$ genes. We assume there are 3 clusters, with true cell proportions $(p_{1,1}, p_{2,1}, p_{3,1}) = (0.6, 0.4, 0)$ for dataset 1 and $(p_{1,2}, p_{2,2}, p_{3,2}) = (0.4, 0, 0.6)$ for dataset 2; simulation details are provided in Web Appendix C.

For both simulations, we investigate prior sensitivity by comparing general priors based on standard hyperparameter values with empirical priors based on hyperparameters specified using initial *bayNorm* estimates (as described in Section 2.2). In addition, to enhance flexibility, we consider both linear and quadratic relationships in the prior model for the mean-variance relationship. This results in four settings for the proposed Norm-HDP model: linear model with general priors (GL), quadratic model with general priors (GQ), linear model with empirical priors (EL) and quadratic model with empirical priors (EQ). In all settings, we perform $T = 8,000$ iterations with a burn-in of 5,000 and thinning of 5; traceplots (shown in Web Appendix C) suggest convergence.

Note that to avoid simulating datasets with empty cells and genes that are not expressed, we generate the true capture efficiencies with a mean of 0.70 which is much higher than the default value of 0.06 for droplet based protocol [Klein et al., 2015]. The capture efficiencies in *bayNorm* are estimated as proportional to cell-specific scaling factors with the global mean set to this default value [Supplementary Note 1 of Tang et al., 2020, and also detailed in Web Appendix B]; thus, the empirical prior based on the *bayNorm* capture efficiencies estimates has prior mean equal to the default value. Due to the identifiability issues discussed in Section 2, recovery of the true capture efficiencies is difficult if the true mean is far from the prior. Hence, for this task, we employ more informative priors by setting the global mean capture efficiency in *bayNorm* to 0.70. In Web Appendix B, we demonstrate good recovery of the true mean capture efficiencies under our Bayesian approach even when the prior mean is slightly misspecified, which is instead problematic for *bayNorm*.

For both simulations, Norm-HDP recovers well the true clustering and mean-dispersion relationships. Results under the EL and EQ setting for Simulation 1 and 2, respectively, are shown in Web Appendix B.4, and the remaining results are shown in Web Appendix B. For both simulations, recovery of the true clustering is robust to the choice of priors and model specification (Web Table B.1); however, for Simulation 2, the quadratic model is better in recovering the true mean-dispersion relationship in comparison to the linear model. In Web Table B.1, we also compare the clustering solutions based on our proposed model (and under the different settings) to three competing methods for clustering scRNA-seq data: 1) Seurat [Satija et al., 2015], 2) CIDR [Lin et al., 2017], and 3) TSCAN [Ji and Ji, 2016]. The VI and adjusted Rand index (ARI) are used to compare the clustering solutions with the truth, where a small value of VI and large value of ARI indicate good performance. In both simulations, Norm-HDP performs the best, followed by Seurat, TSCAN and CIDR.

Posterior predictive checks are presented in Web Appendix B. For the simulated and replicated datasets, we use local polynomial regression to estimate the relationship between 1) the mean against the standard deviation of the log shifted counts and 2) the log mean counts against the drop-out probabilities. These relationships are similar for the simulated and replicated datasets, highlighting the sensible fit of the proposed model.

4.2 Simulation 3

For Simulation 3, we generate 20 replicated sets of data, with $C_1 = 300$ and $C_2 = 400$ cells, for dataset 1 and 2, respectively, with $G = 150$ genes. We assume a total of 3 cell subtypes, with proportions $(p_{1,1}, p_{2,1}, p_{3,1}) = (0.8, 0.2, 0)$ and $(p_{1,2}, p_{2,2}, p_{3,2}) = (0.8, 0, 0.2)$ for dataset 1 and 2, respectively. In addition, we assume that the first 70 percent of the genes are both DE and DD, and remaining genes are both non-DE and non-DD. Unique parameters and allocation variables used to simulate each set of data are identical across replicates. We also assume that the mean expressions $(\mu_{j,g})$ for DE genes follows a log-normal distribution with log-mean m_j for each cluster j and $m_{1:J} = (-3, 5, 8)$. The true relationship between mean and dispersions is assumed to be linear on the log-scale. Simulation details are provided in Web Appendix B. MCMC set-ups are the same as for the previous simulations but under the empirical linear setting only. Figure 4 shows that Norm-HDP recovers well the true mean and dispersion parameters (result based on single set of data). In addition, heat-maps for the true and estimated latent counts show similar patterns (Web Appendix B).

Using the global marker gene detection method proposed in Section 3.3, the range of the FDR, across the 20 replicated sets of data, corresponding to the mean expressions is $(0, 0.047)$ and dispersions is $(0, 0.028)$, hence Norm-HDP is sufficient in detecting the true global marker genes. Relationships between mean absolute LFCs and tail probabilities for a single set of data are shown in Web Figure B.5, in which case the FDR is 0 and 0.019 for the mean expressions and dispersions, respectively.

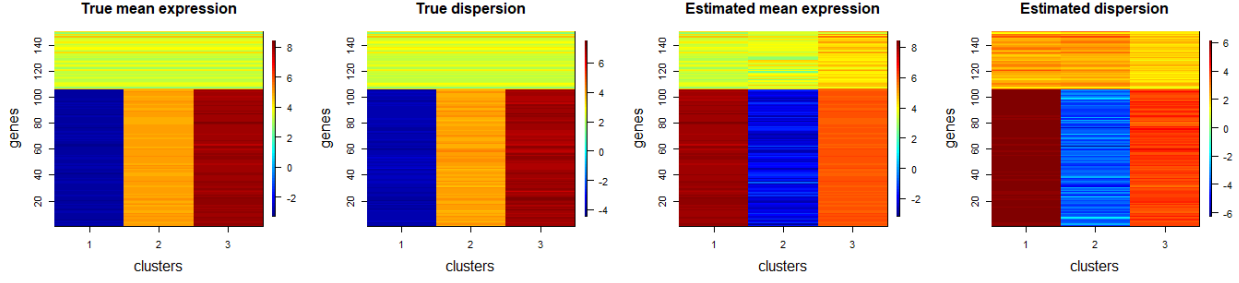


Figure 4: Heat-maps for true and posterior mean of the mean and dispersion parameters (on the log scale), with rows representing genes and columns representing clusters. Note that only the first 70% of genes are DD and DE. True values and posterior estimates of the unique parameters are similar.

5 Experimental Data on Embryonic Cell Development

For posterior inference, we run three parallel MCMC chains with $T = 10,000$ iterations, burn-in of 4,500, and thinning of 5. For robustness to non-linearity, we focus on the quadratic model for the mean-variance relationship with empirical priors and fix the truncation level to $J = 15$. Traceplots demonstrating mixing and convergence are shown in Web Appendix C. In all posterior samples, the number of occupied components is less than 15, thus $J = 15$ provides a sufficient level of truncation. Indeed, the posterior mean of α_0 is 5.18, which is small enough to suggest that the shared cell-subtype proportions of some components may be close to zero. The posterior mean of α is 5.95, suggesting that there is variability in the dataset-specific cell-subtype proportions between the control and mutant groups.

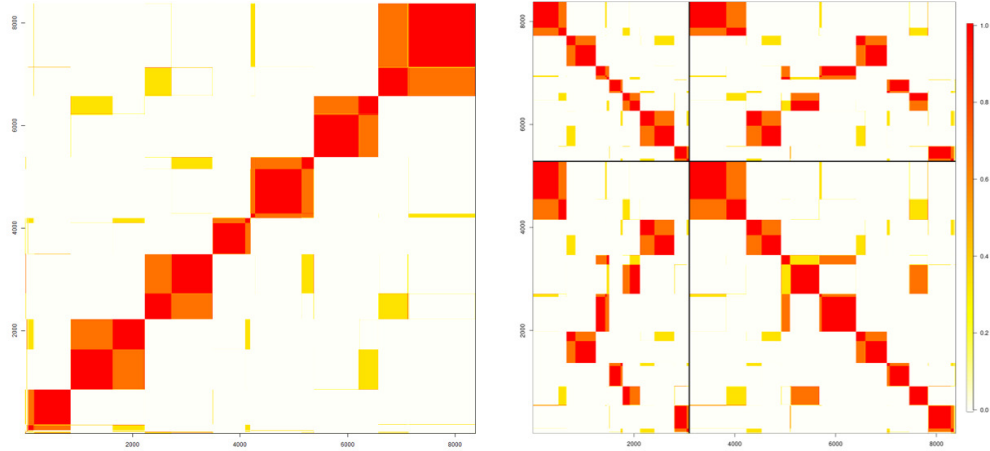


Figure 5: Left: posterior similarity matrix without distinguishing between cells from different datasets. Right: posterior similarity matrix, grouped by HET and HOM. Bottom-Left: the number of cells within each cluster.

A heatmap of the posterior similarity matrix in Figure 5 provides a visualization of the clustering structure and its uncertainty, both within and across conditions. The estimated clustering which minimizes the variation of information contains 8 clusters, all of which are shared between HET and HOM; while this clustering estimate is clearly observed in Figure 5, there is also some apparent uncertainty on whether to further split some clusters. To further study the clustering estimate and its differences between the control and mutant group, we define a cluster as *stable* if the proportion of HET and HOM cells in that cluster is close to the overall proportion, and *under-represented/over-represented* in the mutant group if the proportion of HOM cells in that cluster is lower/greater than the overall proportion. Under this definition, clusters 1, 4, 7 are *stable*, clusters 2 and 6 are *under-represented* in the mutant group, and remaining clusters 3, 5, 8 are *over-represented* in the mutant group. For all clusters, posterior relationships between the estimated mean expressions and dispersions are roughly quadratic and monotonically increasing on the log-scale, and the estimated regression parameters (b) and variance (α_ϕ^2) are sensible in describing the relationship (Web Appendix C). Focusing on

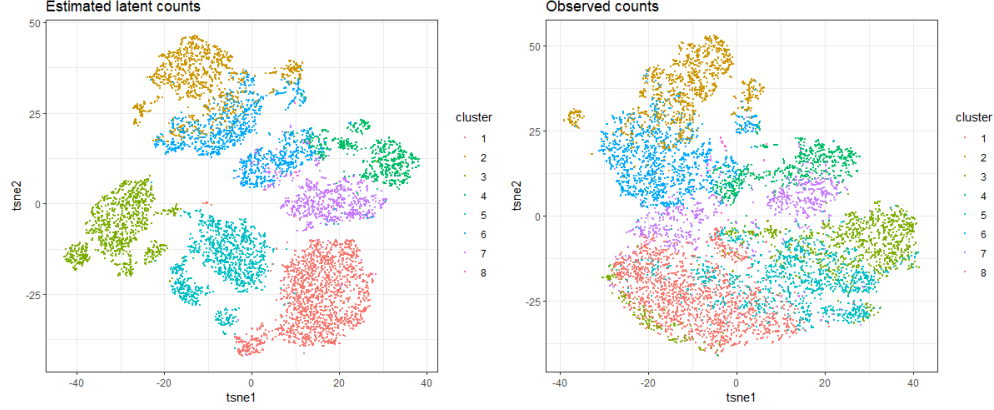


Figure 6: t-SNE plot for the posterior estimated latent counts (Left) and observed counts (Right). Cells from different clusters are shown in different colours.

the estimated capture efficiencies, there are no clear differences across clusters (Web Appendix C), with the exception of the small group of cells in cluster 8, which are mostly from the mutant group and have higher capture efficiencies.

5.1 Global Marker Genes

The detected global marker genes for differential expression and dispersion (with $\tau_0 = 2.5$ and $\omega_0 = 2.5$) are summarized in Web Appendix C and Figure 7. In this case, 47% of genes are global markers for DE and 10% of genes are global markers for DD. To visualize the detected global marker genes across clusters, we include heat-maps of the posterior mean of the cluster-specific parameters, with rows representing genes (reordered by gene-wise tail probabilities) and columns representing clusters. Further, to highlight the differences across clusters, we also observe the relative (when compared with the mean across all clusters) value of cluster-specific parameters for the global marker genes across all clusters. We can observe that cluster 2, which is under-represented in the mutant group, has a distinct pattern across many global marker genes. In addition, the small cluster 8 of mostly HOM cells, appears to have slightly higher expression levels for genes that are lowly expressed in other clusters and, in general, higher dispersion parameters across many global DD genes. Genes with the top 20 highest tail probabilities and absolute log-fold change are listed in Web Appendix Section C.3 for both DE and DD.

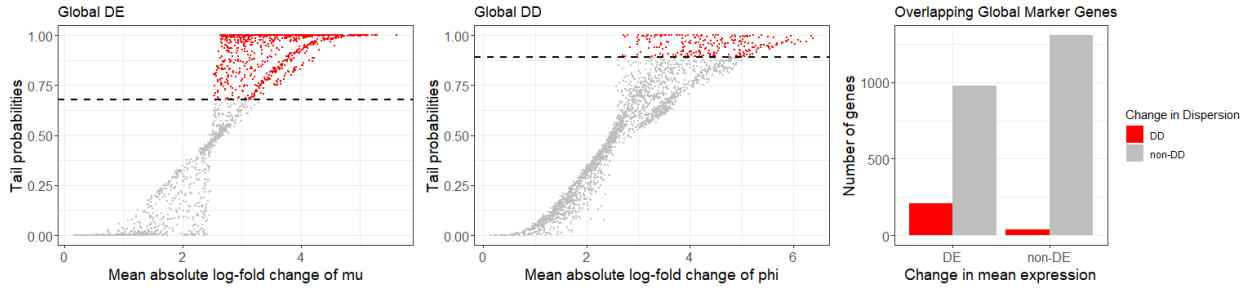


Figure 7: Relationship between mean absolute LFCs and tail probabilities, and a summary of the number of genes with multiple global features.

5.2 Local Marker Genes

For each cluster, we detect local marker genes to identify distinct gene expression patterns in the current cluster in comparison with all other clusters. In the following analysis, we set the threshold values to 0.8 for computing the corresponding tail probabilities. Web Appendix C includes plots of the absolute LFC against tail probabilities together with summary plots. We observe that the under-represented cluster 2 and the small, over-represented cluster 8 have high numbers of local marker genes in terms of both DE and DD. For DE, 163 genes are classified as local DE genes for more than one cell-type and gene 'Lingo1' is classified as a local DE gene for the most cell-types (four cell-types). For DD, 51 genes are classified as local DD genes for more than one cell-type and gene '2310067P03Rik' is classified as a local

DD gene for the most cell-types (four cell-types). Heat-maps of the estimated mean expressions and dispersions for local marker genes are shown in Web Appendix C. We observe that the local marker DE genes for the under-represented cluster 2 tend to be more highly expressed in this cluster. For the small, over-represented cluster 8, the local DE genes tend to be lowly expressed in all other clusters, with slightly higher expression in cluster 8, and most of the local DD genes have higher dispersions (less over-dispersion). In addition, for the remaining clusters 1 and 3-7, most local DD genes have smaller dispersions, thus, these genes are over-dispersed in the corresponding clusters. Genes with the top 10 highest tail probabilities and absolute log-fold change for each cluster are listed in tables in Web Appendix Section C.4 for both DE and DD.

5.3 Posterior Estimated Latent Counts

We compute the posterior estimated latent counts for all cells and compare between different clusters. Figure 8 provides a heat-map of the estimated latent counts; cells are ordered by the clustering estimate, with solid vertical lines separating cells from different clusters and dashed vertical lines separating HET and HOM within cluster. Genes are reordered by global DE tail probabilities, with global DE genes above the horizontal line. Corresponding figures for the observed counts are shown in Web Appendix C. For each gene, posterior estimated latent counts and observed counts for cells within each clusters are similar, and clear differences are observed across cells from different clusters.

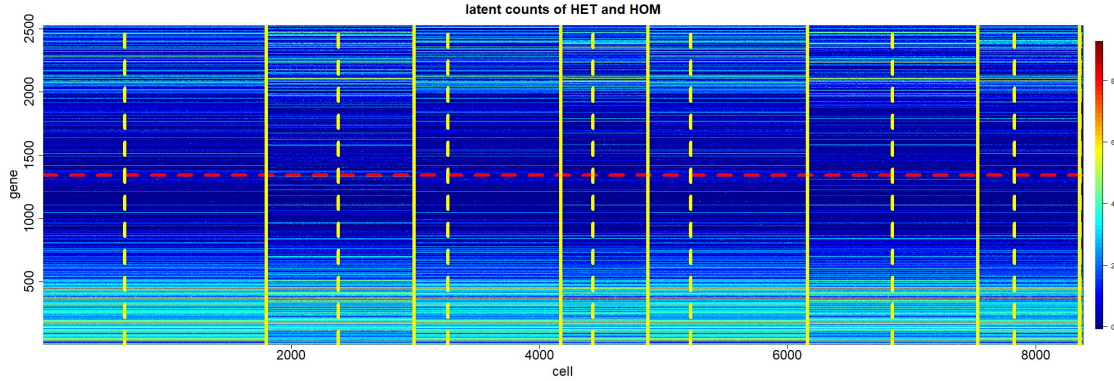


Figure 8: Heat-map of posterior estimated latent gene-counts for HET and HOM. Genes are reordered by global DE tail probabilities, genes above the red horizontal line are global DE, and vice versa. Cells for reordered by the point estimate of posterior allocations. Cells from different clusters are separated by solid lines and cells from different datasets are separated by dashed lines.

In addition, we use t-SNE (a commonly used dimensional reduction method for visualising gene expressions) to visualize similarities between cells within each cluster and differences across clusters (Web Appendix C). Applying t-SNE to the posterior estimated latent counts for genes which are global DE and DD shows a clear separation between clusters (Figure 5).

5.4 Important Genes

Further findings and discussions on the *important* genes that were suspected to show differences across clusters and conditions can be found in Web Appendix D.

5.5 Posterior Predictive Checks

To assess the fit of the proposed Norm-HDP model to the experimental data, we carry out mixed posterior predictive checks, as described in main article Section 3.4. For a single replicated dataset, we compares key statistics and their relationships for the observed and replicated dataset. Namely, the statistics are the mean, standard deviation, and proportion of dropouts for each gene. The statistics of the replicated dataset match well the observed data, highlighting the sensible fit to the data (Figure 9).

For multiple replicates, we show the fitted relationship between 1) the mean and standard deviation of the log shifted counts and 2) the log of the mean counts and proportion of dropouts for the observed dataset and the replicated datasets; the relationships are similar, further supporting the model fit (Web Appendix C).

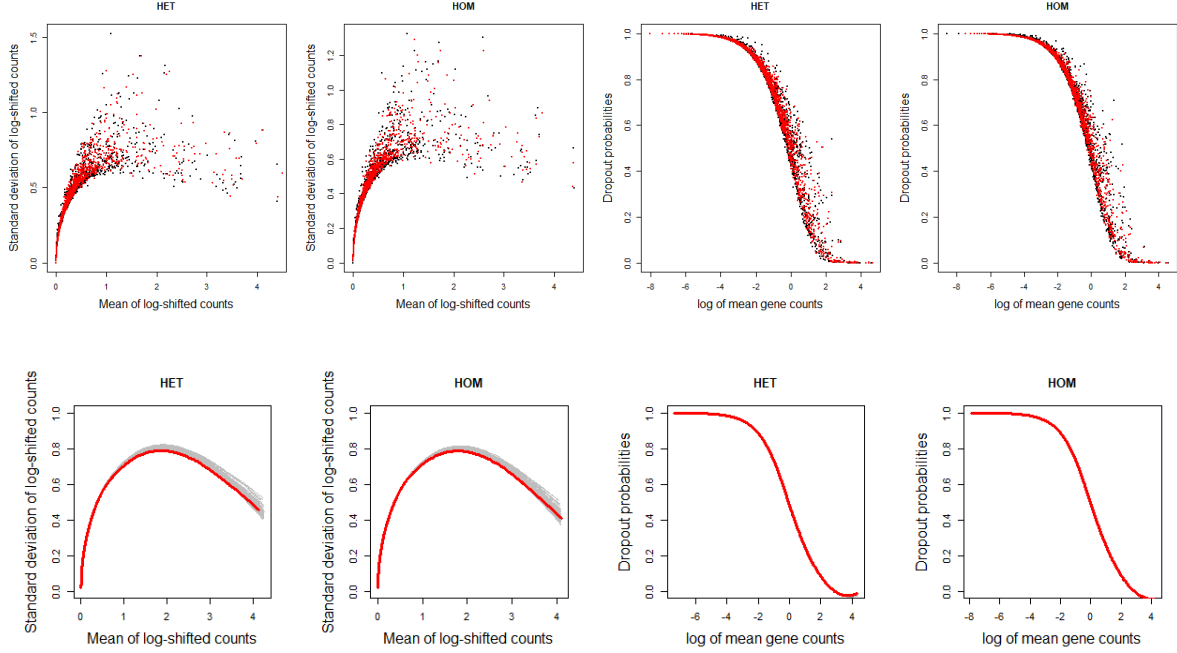


Figure 9: Posterior predictive checks for the experimental data. Row 1: comparing the relationships between key statistics (namely, the mean, standard deviation, and dropout probability) for the observed dataset (in red) and the replicated dataset (in black). Row 2: comparison of the fitted relationships (using polynomial regression), with observed dataset in red and replicated datasets in grey.

6 Discussion

In this article, we have constructed an integrated Bayesian model for simultaneous normalization, imputation, and clustering of multiple single-cell RNA-sequencing datasets across different conditions. In this high-dimensional setting, our hierarchical Bayesian framework allows borrowing of information across conditions as well as measures of uncertainty in the estimated clustering. In simulated datasets, our proposed Norm-HDP model is robust and able to recover the true parameters and clustering, as well detect correctly the marker genes.

In the experimental dataset, the model estimates a total of eight clusters, which are all shared in the control and mutant conditions (with some uncertainty on further splitting some clusters). Certain clusters are under or over represented when PAX6 is knocked out, suggesting differences in cell-subtype proportions across the control and mutant conditions. Most *important* genes that were suspected to show differences across clusters and conditions are identified as marker genes, and additional marker genes have been detected (to be further investigated in future work). We note that tamoxifen administration was carried out at day E9.5, with embryos sacrificed and dissected at day E13.5. Future work will validate and explore additional data collected at day E14.5, which is anticipated to have stronger differences when PAX6 is knocked out.

For posterior inference, we have developed a Gibbs sampling algorithm, which produces asymptotically exact posterior samples. However, a larger number of iterations may be required, and particularly for scRNA-seq data, where the number of cells and genes are typically in the thousands. In future work, we are developing a variational Bayes approximation [Hughes et al., 2015] for faster, approximate inference. Other potential model extensions include cluster-specific mean-dispersion relationships for increased flexibility, as well as priors for clustering beyond the HDP [Argiento et al., 2020].

Acknowledgements

We thank Dr. Tan, Prof. Price, Prof. Mason, Dr. Kozic and their team for providing the datasets, as well as for the insightful descriptions, motivations, suggestions and comments. We also thank Dr. Catalina Vallejos at the MRC Human Genetics Unit, University of Edinburgh for valuable suggestions and comments.

Supporting Information

Web Appendices referenced in Sections 2.2, 3, 4, 5, and 6 are available with this paper at the Biometrics website on Wiley Online Library. All code for model implementation and analysis is publicly available through the Github repository (<https://github.com/jinluliu550/normHDP>), along with the simulated data (Section 4).

References

- R. Argiento, A. Cremaschi, and M. Vannucci. Hierarchical normalized completely random measures to cluster grouped data. *Journal of the American Statistical Association*, 115(529):318–333, 2020.
- P. Brennecke, S. Anders, J.K. Kim, A. Kolodziejczyk, X. Zhang, and V. Proserpio, et al. Accounting for technical noise in single-cell RNA-seq experiments. *Nature Methods*, 10(11):1093, 2013.
- I.M. Cabellaro, M.N. Manuel, M. Molinek, I.Q. Urzainqui, D. Mi, and T. Shimogori, et al. Cell-Autonomous Repression of Shh by Transcription Factor Pax6 Regulates Diencephalic Patterning by Controlling the Central Diencephalic Organizer. *Cell Reports*, 8:1405–1418, 2014.
- M.C.P. de Souto, I.G. Costa, D.S.A. de Araujo, T.B. Ludermir, and A. Schliep. Clustering cancer gene expression data: a comparative study. *BMC Bioinformatics*, 9(1):1–14, 2008.
- T. Duan, J.P. Pinto, and X. Xie. Parallel clustering of single cell transcriptomic data with split-merge sampling on Dirichlet process mixtures. *Bioinformatics*, 35(6):953–961, 2019.
- N. Eling, A.C. Richard, S. Richardson, J.C. Marioni, and C.A. Vallejos. Correcting the mean-variance dependency for differential variability testing using single-cell RNA sequencing data. *Cell Systems*, 7(3):284–294, 2018.
- M. Ester, H.P. Kriegel, J. Sander, and X. Xu. A Density-Based Algorithm for Discovering Clusters in Large Spatial Databases with Noise. *AAAI Press*, 96:226–231, 1996.
- T.S. Ferguson. A Bayesian analysis of some nonparametric problems. *The Annals of Statistics*, pages 209–230, 1973.
- G. Finak, A. McDavid, and M. Yajima. Mast: a flexible statistical framework for assessing transcriptional changes and characterizing heterogeneity in single-cell RNA-sequencing data. *Genome Biology*, 16(278):1–13, 2015.
- S.V. Gassen, B. Callebaut, M. Helden, B. Lambrecht, P. Demmester, and T. Dhaene, et al. Flowsom: using self-organizing maps for visualization and interpretation of cytometry data. *Cytometry A.*, 7(87):636–645, 2015.
- J.E. Griffin and D.A. Stephens. Advances in Markov chain Monte Carlo. In *Bayesian Theory and Applications*, pages 104–144. Oxford University Press Oxford, 2013.
- M. Guo, S.H. Wang, S. Potte, J.A. Whitsett, and Y. Xu. SINCERA: A Pipeline for Single-Cell RNA-Seq Profiling Analysis. *PLOS Computational Biology*, 11(11), 2015.
- M. Hughes, D.I. Kim, and E. Sudderth. Reliable and scalable variational inference for the hierarchical Dirichlet process. In *Artificial Intelligence and Statistics*, pages 370–378. PMLR, 2015.
- H. Ishwaran and L.F. James. Gibbs sampling methods for stick-breaking priors. *Journal of the American Statistical Association*, 96(453):161–173, 2001.
- H. Ishwaran and M. Zarepour. Exact and approximate sum representations for the Dirichlet process. *Canadian Journal of Statistics*, 30(2):269–283, 2002.
- Z. Ji and H. Ji. TSCAN: pseudo-time reconstruction and evaluation in single-cell RNA-seq analysis. *Nucleic Acids Res.*, 13(44), 2016.
- L. Jiang, H. Chen, L. Pinello, and G.C. Yuan. GiniClust: detecting rare cell types from single-cell gene expression data with Gini index. *Genome Biology*, 17(144), 2016.
- J.F.C. Kingman. Random discrete distributions. *Journal of the Royal Statistical Society: Series B*, 37(1):1–15, 1975.
- V. Kiselev, K. Kirschner, M.T. Schaub, T. Andrews, A. Yiu, and T. Chandra, et al. SC3: consensus clustering of single-cell RNA-seq data. *Nat Methods.*, 5(14):483–486, 2017.
- V. Kiselev, T. Andrews, and M. Hemberg. Challenges in unsupervised clustering of single-cell RNA-seq data. *Genetics*, 20:273–282, 2019.
- A.M. Klein, L. Mazutis, I. Akartuna, N. Tallapragada, A. Veres, and V. Li, et al. Droplet barcoding for single-cell transcriptomics applied to embryonic stem cells. *Cell*, 161(5):1187–1201, 2015.
- K.D. Korthauer, L.F. Chu, M.A. Newton, Y. Li, J. Thomson, and Ron. Stewart, et al. A statistical approach for identifying differential distributions in single-cell RNA-seq experiments. *Genome Biology*, 17(1):1–15, 2016.

- A. Lewin, N. Bochkina, and S. Richardson. Fully Bayesian Mixture Model for Differential Gene Expression: Simulation and Model Checks. *Statistical Applications in Genetic and Molecular Biology*, 6, 2007.
- P. Lin, M. Troup, and J.W.K. Ho. CIDR: Ultrafast and accurate clustering through imputation for single-cell RNA-seq data. *Genome Biology*, 1(18), 2017.
- M.N. Manuel, K.B. Tan, Z. Kozic, M. Molinek, T.S. Marcos, and M.F.A. Razak, et al. PAX6 limits the competence of developing cerebral cortical cells to respond to inductive intercellular signals. *PLOS Biology*, 2022. *In press*.
- C.P. Martinez-Jimenez, N. Eling, H.C. Chen, C.A. Vallejos, A.A. Kolodziejczyk, and F. Connor, et al. Aging increases cell-to-cell transcriptional variability upon immune stimulation. *Science*, 355(6332):1433–1436, 2017.
- D. Mi, Y.T. Huang, D. Kleinjan, J.O. Mason, and D.J. Price. Identification of Genomic Regions Regulating Pax6 Expression in Embryonic Forebrain Using YAC Reporter Transgenic Mouse Lines. *PLoS ONE*, 8(11), 2013.
- J. Miller and D. Dunson. Robust Bayesian Inference via Coarsening. *Journal of American Statistical Association*, 114(527):1113–1125, 2015.
- J. Miller and M. Harrison. Inconsistency of Pitman–Yor Process Mixtures for the Number of Components. *Journal of Machine Learning Research*, 15:3333–3370, 2013.
- A. Olsson, M. Venkatasubramanian, V.K. Chaudhri, B.J. Aronow, N. Salomonis, and H. Singh, et al. Single-cell analysis of mixed-lineage states leading to a binary cell fate choice. *Nature*, (537):698–702, 2016.
- R. Petegrosso, Z. Li, and R. Kuang. Machine learning and statistical methods for clustering single-cell RNA-sequencing data. *Bioinformatics*, 21(4):1209–1223, 2020.
- S. Prabhakaran, E. Azizi, A. Carr, and D. Pe’er. Dirichlet process mixture model for correcting technical variation in single-cell gene expression data. In *International Conference on Machine Learning*, pages 1070–1079. PMLR, 2016.
- X. Qiu, Q. Miao, T. Tang, L. Wang, R. Chawla, and H. Pliner, et al. Reversed graph embedding resolves complex single-cell trajectories. *Nature Methods*, 4(10):979–982, 2017.
- D. Risso, F. Perraudeau, S. Gribkova, S. Dudoit, and J.P. Vert. A general and flexible method for signal extraction from single-cell RNA-seq data. *Nature Communications*, 9(1):284, 2018.
- A. Rodriguez, D. Dunson, and A. Gelfand. The Nested Dirichlet Process. *Journal of the American Statistical Association*, 103(483):1134–1154, 2008.
- J. Rousseau and K. Mengersen. Asymptotic behaviour of the posterior distribution in overfitted mixture models. *Journal of the Royal Statistical Society. Series B (Statistical Methodology)*, 73(5):689–710, 2011.
- R. Satija, J.A. Farrell, D. Gennert, A.F. Schier, and A. Regev. Spatial reconstruction of single-cell gene expression data. *Nat Biotechnol.*, 33(5):495–502, 2015.
- A. Senabouth, S. Lukowski, J. Hernandez, S. Andersona, X. Mei, and Q. Nguyen, et al. ascend: R package for analysis of single cell RNA-seq data. *bioRxiv*, 2017.
- T. Stuart, A. Butler, P. Hoffman, C. Hafemeister, E. Papalexi, and W.M Mauck III, et al. Comprehensive Integration of Single-Cell Data. *Cell*, 177:1888–1902, 2019. doi: 10.1016/j.cell.2019.05.031. URL <https://doi.org/10.1016/j.cell.2019.05.031>.
- Z. Sun, T. Wang, K. Deng, X.F. Wang, R. Lafyatis, and Y. Ding, et al. DIMM-SC: a Dirichlet mixture model for clustering droplet-based single cell transcriptomic data. *Bioinformatics*, 34(1):139–146, 2018.
- W. Tang, F. Bertaux, P. Thomas, C. Stefanelli, M. Saint, and S. Marguerat, et al. bayNorm: Bayesian gene expression recovery, imputation and normalization for single-cell RNA-sequencing data. *Bioinformatics*, 36(4):1174–1181, 2020.
- Y.W. Teh, M.I. Jordan, M.J. Beal, and D.M. Blei. Hierarchical Dirichlet processes. *Journal of the American Statistical Association*, 101(476), 2006.
- C. Vallejos, D. Risso, A. Scialdone, S. Dudoit, and J.C. Marioni. Normalizing single-cell RNA sequencing data: challenges and opportunities. *Nature Methods*, 14(6):565, 2017.
- C.A. Vallejos, J.C. Marioni, and S. Richardson. BASiCS: Bayesian analysis of single-cell sequencing data. *PLoS Computational Biology*, 11(6), 2015.
- C.A. Vallejos, S. Richardson, and J.C. Marioni. Beyond comparisons of means: understanding changes in gene expression at the single-cell level. *Genome Biology*, 17(1):70, 2016.
- S. Wade and Z. Ghahramani. Bayesian Cluster Analysis: Point Estimation and Credible Balls (with Discussion). *Bayesian Analysis*, 13(2):559–626, 2018.

- Q. Wu and X. Luo. A nonparametric Bayesian approach to simultaneous subject and cell heterogeneity discovery for single cell RNA-seq data. *arXiv preprint arXiv:1912.08050*, 2019.
- Y. Yang, R. Huh, H.W. Culpepper, Y. Lin, M.I. Love, and Y. Li. SAFE-clustering: Single-cell aggregated (from ensemble) clustering for single-cell RNA-seq data. *bioRxiv*, 2017.
- A. Zeisell, A.B. Munoz-Manchado, S. Codeluppi, P. Lonnerberg, G.L. Manno, and A. Jureus, et al. Cell types in the mouse cortex and hippocampus revealed by single-cell RNA-seq. *Science*, 347(6226):1138–1142, 2015.
- J.M. Zhang, J. Fan, H.C. Fan, D. Rosenfeld, and D.N. Tse. An interpretable framework for clustering single-cell RNA-Seq datasets. *BMC Bioinformatics*, 19(93):1–12, 2018.
- J. Zurauskiene and C. Yau. pcaReduce: hierarchical clustering of single cell transcriptional profiles. *BMC Bioinformatics*, 1(17), 2016.

SUPPORTING INFORMATION FOR SHARED DIFFERENTIAL CLUSTERING ACROSS SINGLE-CELL RNA SEQUENCING DATASETS WITH THE HIERARCHICAL DIRICHLET PROCESS

Jinlu Liu

School of Mathematics
University of Edinburgh
Jinlu.Liu@ed.ac.uk

Sara Wade

School of Mathematics
University of Edinburgh
Sara.Wade@ed.ac.uk

Natalia Bochkina

School of Mathematics
University of Edinburgh
N.bochkina@ed.ac.uk

January 5, 2023

ABSTRACT

In Web Appendix A, we describe the MCMC algorithm for posterior inference; explain the derivation of *bayNorm* estimates of the capture efficiencies; give details of the computation of *global* and *local* marker genes based on estimated mean expressions and dispersions; demonstrate the effect of change concentration parameters on dataset-specific allocation proportions; and derive the posterior distribution of latent counts. In Web Appendix B, we include the details of simulated examples, including data generation, results and additional experiment to investigate misspecification of the mean capture efficiency. In Web Appendix C, we provide further details on the PAX6 data analysis, including the filtering process; MCMC summaries; *global* marker genes; *local* marker genes; t-SNE plots and posterior predictive checks. In Web Appendix D, we show the results corresponding to the ‘important’ genes. In Web Appendix E, we give a full discussion of our findings and suggest potential further research topics.

Contents

Appendices	2
A Web Appendix A: Posterior Inference, Capture Efficiency Estimates, Global Marker Genes and Concentration Parameters	3
A.1 Mean-dispersion Hyperparameters	3
A.2 Allocation Variables	4
A.3 Dataset-specific Component Probabilities	5
A.4 Component Probabilities	5
A.4.1 Adaptive Metropolis-Hastings for \mathbf{p}	6
A.5 Concentration Parameters	7
A.5.1 Adaptive Metropolis-Hastings for α	7
A.6 Unique Parameters	8
A.6.1 Adaptive Metropolis Hastings for μ and ϕ	8
A.7 Capture Efficiencies	9
A.7.1 Adaptive Metropolis-Hastings for β	9
A.8 bayNorm Estimates of the Capture Efficiencies	10
A.9 Marker Genes	10
A.10 Latent Counts	11
B Web Appendix B: Simulations	11
B.1 Simulation 1: Data Generation	11
B.2 Simulation 2: Data Generation	11
B.3 Simulation 3: Data Generation	12
B.4 Simulations 1 and 2: Results	12
B.5 Simulation 3: Results	16
B.6 Additional Simulations with Misspecified Mean Capture Efficiencies	17
C Web Appendix C: PAX6 Data Analysis	18
C.1 Filtering Process	18
C.2 Results	19
C.3 Global Marker Genes	23
C.4 Local Marker Genes	27
C.5 Posterior Estimated Latent Counts	30
C.6 Posterior Predictive Checks	31
D Web Appendix D: Important Genes	31
E Web Appendix E: Discussion	35

A Web Appendix A: Posterior Inference, Capture Efficiency Estimates, Global Marker Genes and Concentration Parameters

In this section, we describe the algorithm for posterior inference with the Norm-HDP model. In the following, we assume the relationship between the mean and dispersion parameters is linear on the log scale. Let $\mathbf{Z} = (z_{c,d})_{c=1,d=1}^{C_d,D}$; $\mathbf{Y} = (y_{c,d,g})_{c=1,d=1,g=1}^{C_d,D,G}$; $\mathbf{p}_d = (p_{1,d}^J, \dots, p_{J,d}^J)$; $\mathbf{p} = (p_1^J, \dots, p_J^J)$; $\beta = (\beta_{c,d})_{c=1,d=1}^{C_d,D}$. The posterior of interest is:

$$\begin{aligned} \pi(\mathbf{Z}, \mathbf{p}_d, \mathbf{p}, \boldsymbol{\mu}_{1:J}^*, \boldsymbol{\phi}_{1:J}^*, \beta, \alpha, \alpha_0, \mathbf{b}, a_\phi^2 | \mathbf{Y}) &\propto \prod_{j=1}^J \prod_{(c,d): z_{c,d}=j} \prod_{g=1}^G \text{NB}(y_{c,d,g} | \mu_{j,g}^* \beta_{c,d}, \phi_{j,g}^*) \\ &\quad * \prod_{j=1}^J \prod_{d=1}^D p_{j,d}^{N_{j,d}} * \prod_{d=1}^D \text{Dir}(\mathbf{p}_d | \alpha \mathbf{p}) * \text{Dir}\left(\mathbf{p} | \frac{\alpha_0}{J}, \dots, \frac{\alpha_0}{J}\right) \\ &\quad * \prod_{j=1}^J \prod_{g=1}^G \text{LN}(\mu_{j,g}^* | 0, a_u^2) \text{LN}(\phi_{j,g}^* | b_0 + b_1 \log(\mu_{j,g}^*), a_\phi^2) \\ &\quad * \prod_{d=1}^D \prod_{c=1}^{C_d} \text{Beta}(\beta_{c,d} | a_d^\beta, b_d^\beta) * \text{Gam}(\alpha | 1, 1) * \text{Gam}(\alpha_0 | 1, 1) \\ &\quad * \text{N}(\mathbf{b} | \mathbf{m}_b, a_\phi^2 \mathbf{V}_b) * \text{IG}(a_\phi^2 | \nu_1, \nu_2), \end{aligned}$$

where $N_{j,d} = \sum_{c=1}^{C_d} \mathbf{1}(z_{c,d} = j)$ is the number of cells in component j in dataset d . A Markov chain Monte Carlo (MCMC) algorithm is developed for full posterior inference. The algorithm is a Gibbs sampler which produces asymptotically exact samples from the posterior by iteratively sampling the parameters in blocks corresponding to the:

- allocation variables $\mathbf{Z} | \mathbf{p}_d, \boldsymbol{\mu}_{1:J}^*, \boldsymbol{\phi}_{1:J}^*, \mathbf{Y}, \beta$,
- dataset-specific component probabilities $\mathbf{p}_d | \mathbf{Z}, \mathbf{p}, \alpha$,
- component probabilities $\mathbf{p} | \mathbf{p}_{1:D}, \alpha_0$,
- unique parameters $\boldsymbol{\mu}_j^*, \boldsymbol{\phi}_j^* | \mathbf{Z}, \mathbf{b}, a_\phi^2, \mathbf{Y}, \beta$,
- concentration parameters $\alpha | \mathbf{p}_{1:D}, \mathbf{p}$ and $\alpha_0 | \mathbf{p}$,
- mean-dispersion hyperparameters $\mathbf{b}, a_\phi^2 | \boldsymbol{\mu}_{1:J}^*, \boldsymbol{\phi}_{1:J}^*$,
- capture efficiencies $\beta | \mathbf{Y}, \mathbf{Z}, \boldsymbol{\mu}_{1:J}^*, \boldsymbol{\phi}_{1:J}^*$.

The complexity of the algorithm is dominated by the update of the allocation variables, which is of order $\mathcal{O}(\text{sum}(C)JG)$. In the following subsections, we describe the update for each block of parameters.

A.1 Mean-dispersion Hyperparameters

The full conditional distribution for the mean-dispersion hyperparameters in the linear case is:

$$\begin{aligned} \pi(\mathbf{b}, \alpha_\phi^2 | \boldsymbol{\mu}_{1:J}^*, \boldsymbol{\phi}_{1:J}^*) &\propto \text{N}(\mathbf{b} | \mathbf{m}_b, \alpha_\phi^2 \mathbf{V}_b) * \text{IG}(\alpha_\phi^2 | v_1, v_2) * \prod_{j=1}^J \prod_{g=1}^G \log \text{N}(\phi_{j,g}^* | b_0 + b_1 \log(\mu_{j,g}^*), \alpha_\phi^2) \\ &\propto \left(\frac{1}{\alpha_\phi^2} \right)^{v_1 + 2 + \frac{JG}{2}} \exp \left(-\frac{1}{\alpha_\phi^2} \left[\frac{1}{2} \sum_{j=1}^J \sum_{g=1}^G (\ln(\phi_{j,g}^*) - b_0 - b_1 \log(\mu_{j,g}^*))^2 + v_2 + \frac{1}{2} [b_0^2 + b_1^2] \right] \right). \quad (1) \end{aligned}$$

Following eq. (1), the full conditional for \mathbf{b} conditioning on α_ϕ^2 is:

$$\pi(\mathbf{b} | \boldsymbol{\mu}_{1:J}^*, \boldsymbol{\phi}_{1:J}^*, \alpha_\phi^2) \propto \exp \left(-\frac{1}{2\alpha_\phi^2} \left[\sum_{j=1}^J \sum_{g=1}^G (\ln(\phi_{j,g}^*) - b_0 - b_1 \log(\mu_{j,g}^*))^2 + [b_0^2 + b_1^2] \right] \right).$$

Hence we have the full conditional:

$$\mathbf{b} | \boldsymbol{\mu}_{1:J}^*, \boldsymbol{\phi}_{1:J}^*, \alpha_\phi^2 \sim \text{N}(\tilde{\mathbf{m}}_b, \alpha_\phi^2 \tilde{\mathbf{V}}_b), \quad (2)$$

where

$$\begin{aligned}\tilde{\mathbf{m}}_b &= \left(\sum_{j=1}^J \tilde{\boldsymbol{\mu}}_j^T \tilde{\boldsymbol{\mu}}_j + I \right)^{-1} \left(\sum_{j=1}^J \tilde{\boldsymbol{\mu}}_j^T \ln(\phi_j^*) \right), \\ \tilde{\mathbf{V}}_b &= \left(\sum_{j=1}^J \tilde{\boldsymbol{\mu}}_j^T \tilde{\boldsymbol{\mu}}_j + I \right)^{-1},\end{aligned}$$

and

$$\ln(\phi_j^*) = \begin{bmatrix} \ln(\phi_{j,1}^*) \\ \vdots \\ \ln(\phi_{j,G}^*) \end{bmatrix}, \quad \tilde{\boldsymbol{\mu}}_j = \begin{bmatrix} 1 & \log(\mu_{j,1}^*) \\ \vdots & \vdots \\ 1 & \log(\mu_{j,G}^*) \end{bmatrix}.$$

And following eq. (1), the full conditional for α_ϕ^2 is:

$$\begin{aligned}\pi(\alpha_\phi^2 | \boldsymbol{\mu}_{1:J}^*, \phi_{1:J}^*) &= \int \pi(\mathbf{b}, \alpha_\phi^2 | \boldsymbol{\mu}_{1:J}^*, \phi_{1:J}^*) d\mathbf{b} \\ &\propto \int \left(\frac{1}{\alpha_\phi^2} \right)^{v_1+1} \exp \left(-\frac{v_2}{\alpha_\phi^2} \right) \left(\frac{1}{\alpha_\phi^2} \right)^{JG/2} \left(\frac{1}{\alpha_\phi^2} \right) \\ &\quad * \exp \left(-\frac{1}{2\alpha_\phi^2} \left[(\mathbf{b} - \tilde{\mathbf{m}}_b)^T \tilde{\mathbf{V}}_b^{-1} (\mathbf{b} - \tilde{\mathbf{m}}_b) - \tilde{\mathbf{m}}_b^T \tilde{\mathbf{V}}_b^{-1} \tilde{\mathbf{m}}_b + \sum_{j=1}^J \ln(\phi_j^*)^T \ln(\phi_j^*) \right] \right) d\mathbf{b}.\end{aligned}$$

Thus, we have:

$$\alpha_\phi^2 | \boldsymbol{\mu}_{1:J}^*, \phi_{1:J}^* \sim \text{IG}(\tilde{v}_1, \tilde{v}_2), \quad (3)$$

where

$$\begin{aligned}\tilde{v}_1 &= v_1 + JG/2, \\ \tilde{v}_2 &= v_2 + \frac{1}{2} \left(\sum_{j=1}^J \ln(\phi_j^*)^T \ln(\phi_j^*) - \tilde{\mathbf{m}}_b^T \tilde{\mathbf{V}}_b^{-1} \tilde{\mathbf{m}}_b \right).\end{aligned}$$

For Gibbs sampling, at each iteration, we first simulate α_ϕ^2 from the Inverse-Gamma distribution in eq. (3) and then conditioned on this value, simulate \mathbf{b} from the Normal distribution in eq. (2). Details are given in Algorithm 1.

Algorithm 1 Simulation of Mean-dispersion Hyperparameters

Require: $\boldsymbol{\mu}_{1:J}^*, \phi_{1:J}^*$

Ensure: $\alpha_\phi^2, \mathbf{b}$

$A \leftarrow$ Identity matrix of dimension 2;

$B \leftarrow$ Zero matrix with 2 rows and 2 column;

$C \leftarrow 0$;

for $j = 1, \dots, J$ **do**

$A = A + \tilde{\boldsymbol{\mu}}_j^T \tilde{\boldsymbol{\mu}}_j$; $B = B + \tilde{\boldsymbol{\mu}}_j^T \ln(\phi_j^*)$; $C = C + \ln(\phi_j^*)^T \ln(\phi_j^*)$;

end for

$\tilde{\mathbf{V}}_b \leftarrow A^{-1}$; $\tilde{\mathbf{m}}_b \leftarrow \tilde{\mathbf{V}}_b A$; $\tilde{v}_1 \leftarrow v_1 + JG/2$; $\tilde{v}_2 \leftarrow v_2 + 1/2 * (C - \tilde{\mathbf{m}}_b^T \tilde{\mathbf{V}}_b^{-1} \tilde{\mathbf{m}}_b)$;

Simulate α_ϕ^2 and \mathbf{b} from the NIG in eq. 3 and 2 using the above parameters.

A.2 Allocation Variables

The full conditional for the allocation variables is:

$$\pi(\mathbf{Z} | \mathbf{P}_{1:D}, \boldsymbol{\mu}_{1:J}^*, \phi_{1:J}^*, \mathbf{y}, \beta) \propto \prod_{j=1}^J \prod_{(c,d): z_{c,d}=j} \prod_{g=1}^G \text{NB}(y_{c,g,d} | \mu_{j,g}^* \beta_{c,d}, \phi_{j,g}^*) \prod_{j=1}^J \prod_{d=1}^D p_{j,d}^{N_{j,d}},$$

where $N_{j,d}$ is the total number of cells in component j in dataset d . Thus, since the allocations are conditionally independent, we have the full conditional of z for cell c in dataset d as:

$$z_{c,d} \sim \text{Cat}(\pi_{c,d,1}, \dots, \pi_{c,d,J}), \quad (4)$$

where $\pi_{c,d,j} = \pi(z_{c,d} = j | \mathbf{P}_{1:D}, \boldsymbol{\mu}_{1:J}^*, \boldsymbol{\phi}_{1:J}^*, \mathbf{Y}, \boldsymbol{\beta})$. To avoid numerical errors, we employ the log-sum trick to compute the probabilities:

$$\pi_{c,d,j} = \frac{\exp(\log(\tilde{\pi}_{c,d,j}) + \log(K))}{\sum_{j=1}^J \exp(\log(\tilde{\pi}_{c,d,j}) + \log(K))}.$$

where

$$\begin{aligned} \tilde{\pi}_{c,d,j} &= \prod_{g=1}^G \text{NB}(y_{c,g,d} | \mu_{j,g}^* \beta_{c,d}, \phi_{j,g}^*) p_{j,d}, \\ \log(K) &= -\max_j \log(\tilde{\pi}_{c,d,j}). \end{aligned}$$

Details are given in Algorithm 2.

Algorithm 2 Simulation of Allocation Variables

Require: $\mathbf{P}_{1:D}, \boldsymbol{\mu}_{1:J}^*, \boldsymbol{\phi}_{1:J}^*, \mathbf{Y}, \boldsymbol{\beta}$

Ensure: \mathbf{Z}

$\mathbf{Z} \leftarrow$ a list of length D ;

for $d = 1, \dots, D$ and $c = 1, \dots, C_d$ **do**

 Compute $\tilde{\pi}_{c,d,j}$ for each j ; and K ,

 Use $\tilde{\pi}_{c,d,j}$ and K to compute $\pi_{c,d,j}$ and simulate $z_{c,d}$ from the Categorical distribution in eq. (4).

end for

A.3 Dataset-specific Component Probabilities

The full conditional distribution for the dataset-specific component probabilities is:

$$\pi(\mathbf{p}_d | \mathbf{Z}, \mathbf{p}, \alpha) \propto \prod_{j=1}^J p_{j,d}^{N_{j,d}} \text{Dir}(\mathbf{p}_d | \alpha \mathbf{p}) \propto \prod_{j=1}^J p_{j,d}^{N_{j,d} + \alpha p_j - 1}.$$

Hence, $\mathbf{p}_d | \mathbf{Z}, \mathbf{p}, \alpha$ follows a Dirichlet distribution with parameters equals to $N_{j,d} + \alpha p_j$, for $j = 1, \dots, J$. Details are given in Algorithm 3.

Algorithm 3 Simulation of Dataset-specific Component Probabilities

Require: $\mathbf{Z}, \mathbf{P}, \alpha$

Ensure: $\mathbf{p}_{1:D}$

$\mathbf{p}_{1:D} \leftarrow$ Matrix with J rows and D columns;

for $d = 1, \dots, D$ **do**

$\tilde{\alpha} \leftarrow \text{table}(\mathbf{Z}_d) + \alpha \mathbf{p}$

 Simulate \mathbf{p}_d from the Dirichlet distribution using the updated parameters $\tilde{\alpha}$.

end for

A.4 Component Probabilities

The full conditional distribution for the component probabilities is:

$$\begin{aligned} \pi(\mathbf{p} | \mathbf{p}_{1:D}, \alpha_0, \alpha) &\propto \text{Dir}(\mathbf{p} | \frac{\alpha_0}{J}, \dots, \frac{\alpha_0}{J}) * \prod_{d=1}^D \text{Dir}(\mathbf{p}_d | \alpha \mathbf{p}) \\ &\propto \left[\prod_{j=1}^J p_j^{\frac{\alpha_0}{J} - 1} \right] \prod_{d=1}^D \frac{1}{B(\alpha \mathbf{p})} \prod_{j=1}^J p_{j,d}^{\alpha p_j} * \mathbf{1} \left(p_j > 0, \forall j, \sum_{j=1}^J p_j = 1 \right). \end{aligned} \quad (5)$$

As the full conditional distribution has no closed-form, we will use adaptive Metropolis-Hastings [Griffin and Stephens, 2013] to obtain posterior samples of \mathbf{p} . The log of the full conditional in eq. (5) can be written as:

$$\log \pi(\mathbf{p} | \dots) = \sum_{j=1}^J \left[\left(\frac{\alpha_0}{J} - 1 \right) \log(p_j) \right] + \sum_{d=1}^D \sum_{j=1}^J [\alpha p_j \log(p_{j,d}) - \log \Gamma(\alpha p_j)] + \text{const.}$$

A.4.1 Adaptive Metropolis-Hastings for \mathbf{p}

In the following, we describe the steps of the adaptive Metropolis-Hastings algorithm.

1. Note that since $p_j > 0$ for all $j = 1, \dots, J$ and $\sum_{j=1}^J p_j = 1$, we apply the following transformation:

$$\mathbf{p} \in \Delta^{J-1} \mapsto \mathbf{x} \in \mathbb{R}^{J-1}$$

where

$$x_j = t(p_j) := \log \left(\frac{p_j}{p_J} \right), \quad j = 1, \dots, J-1.$$

Note that the reverse of the transformation is:

$$p_j = \frac{e^{x_j}}{1 + \sum_{j=1}^{J-1} e^{x_j}}, \quad j = 1, \dots, J-1.$$

2. For $n \leq 100$, \mathbf{x}_{new} is simulated from $N(\mathbf{x}_{old}, \mathbf{I}_d)$. If $n > 100$, \mathbf{x}_{new} is simulated from $N(\mathbf{x}_{old}, 2.4^2/d * (\Sigma_{n-1} + \epsilon \mathbf{I}_d))$, where Σ_{n-1} is the current estimate of covariance structure of \mathbf{x} based on the first $n-1$ samples; d is the length of the parameters of interest, i.e. $d = J-1$; and an epsilon is small constant, i.e. $\epsilon = 0.01$.
3. To avoid re-computing Σ_n at each iteration, we compute Σ_n based on two statistics: $\tilde{\mathbf{S}}_n$ and \mathbf{m}_n , which can be sequentially updated. These statistics are defined as:

$$\tilde{\mathbf{S}}_n = \begin{bmatrix} \sum_{i=1}^n x_{1,i}^2 & \sum_{i=1}^n x_{1,i} x_{2,i} & \cdots & \sum_{i=1}^n x_{1,i} x_{J-1,i} \\ \vdots & \vdots & \ddots & \vdots \\ \sum_{i=1}^n x_{J-1,i} x_{1,i} & \sum_{i=1}^n x_{J-1,i} x_{2,i} & \cdots & \sum_{i=1}^n x_{J-1,i}^2 \end{bmatrix},$$

$$\mathbf{m}_n = \left[\sum_{i=1}^n x_{1,i}, \dots, \sum_{i=1}^n x_{J-1,i} \right]^T.$$

We can express Σ_n as:

$$\Sigma_n = \frac{1}{n-1} \tilde{\mathbf{S}}_n - \frac{n}{n-1} \mathbf{m}_n \mathbf{m}_n^T,$$

where we sequentially update the required statistics:

$$\begin{aligned} \tilde{\mathbf{S}}_n &= \tilde{\mathbf{S}}_{n-1} + \mathbf{x}_n \mathbf{x}_n^T; \\ \mathbf{m}_n &= \left(1 - \frac{1}{n} \right) \mathbf{m}_n + \frac{1}{n} \mathbf{x}_n. \end{aligned}$$

4. To evaluate the proposal distribution, we are required to compute the Jacobian of the transformation. More specifically, the proposal is:

$$q_n(\mathbf{p}_{new} | \mathbf{p}_{old}) = q_n(t(\mathbf{p}_{new}) | t(\mathbf{p}_{old})) |J_{t(\mathbf{p}_{new})}|,$$

where

$$\begin{aligned} J_{t(\mathbf{p})} &= \begin{pmatrix} \frac{dt_1}{dp_1} & \frac{dt_2}{dp_1} & \cdots & \frac{dt_{J-1}}{dp_1} \\ \vdots & \vdots & \ddots & \vdots \\ \frac{dt_1}{dp_{J-1}} & \frac{dt_2}{dp_{J-1}} & \cdots & \frac{dt_{J-1}}{dp_{J-1}} \end{pmatrix} \\ &= \begin{pmatrix} \frac{1}{p_J} & \cdots & \frac{1}{p_J} \\ \vdots & \ddots & \vdots \\ \frac{1}{p_J} & \cdots & \frac{1}{p_J} \end{pmatrix} + \begin{pmatrix} \frac{1}{p_1} & 0 & \cdots & 0 \\ 0 & \frac{1}{p_2} & \ddots & 0 \\ \vdots & \vdots & \ddots & 0 \\ 0 & 0 & \cdots & \frac{1}{p_{J-1}} \end{pmatrix} = B + A. \end{aligned}$$

Since $\det(A + B) = \det(A) + \det(B) + \text{Tr}(A^{-1}B) \det(A)$, and in our case, we have $\det(B) = 0$ and $\det(A) = \prod_{j=1}^{J-1} \frac{1}{p_j}$, hence $\det(A + B) = \prod_{j=1}^{J-1} \frac{1}{p_j} + [1 - p_J] \prod_{j=1}^J \frac{1}{p_j} = \prod_{j=1}^J \frac{1}{p_j}$. And taking the log of the determinant of the Jacobian, we have

$$\log \det J_{\mathbf{t}(\mathbf{P})} = \log \left[\prod_{j=1}^J \frac{1}{p_j} \right] = - \sum_{j=1}^J \log(p_j).$$

5. Next, we compute the acceptance probability:

$$\alpha(\mathbf{p}_{new}, \mathbf{p}_{old}) = \min\{1, \exp(\tilde{\alpha}(\mathbf{p}_{new}, \mathbf{p}_{old}))\},$$

where

$$\begin{aligned} \tilde{\alpha}(\mathbf{p}_{new}, \mathbf{p}_{old}) &= \log \left[\frac{\pi(\mathbf{p}_{new}) q_n(\mathbf{p}_{old}|\mathbf{p}_{new})}{\pi(\mathbf{p}_{old}) q_n(\mathbf{p}_{new}|\mathbf{p}_{old})} \right] = \log \left[\frac{\pi(\mathbf{p}_{new}) |J_{\mathbf{t}(\mathbf{p}_{old})}|}{\pi(\mathbf{p}_{old}) |J_{\mathbf{t}(\mathbf{p}_{new})}|} \right] \\ &= \log \left[\frac{\pi(\mathbf{p}_{new})}{\pi(\mathbf{p}_{old})} \right] - \sum_{j=1}^J \log(p_{old,j}) + \sum_{j=1}^J \log(p_{new,j}), \end{aligned}$$

and $\pi(\cdot)$ is the density of the target distribution.

A.5 Concentration Parameters

The full conditional distribution for α is:

$$\begin{aligned} \pi(\alpha|\mathbf{p}_{1:D}, \mathbf{p}) &\propto \text{Gam}(\alpha|1, 1) * \prod_{d=1}^D \text{Dir}(\mathbf{p}_d|\alpha\mathbf{p}) \propto \exp(-\alpha) \prod_{d=1}^D \frac{1}{B(\alpha\mathbf{p})} \prod_{j=1}^J p_{j,d}^{\alpha p_j} \\ &\propto \exp(-\alpha) \prod_{d=1}^D \frac{\Gamma(\alpha)}{\prod_{j=1}^J \Gamma(\alpha p_j)} \prod_{j=1}^J p_{j,d}^{\alpha p_j} * \mathbf{1}(\alpha > 0). \end{aligned} \quad (6)$$

The full conditional distribution for α_0 is:

$$\begin{aligned} \pi(\alpha_0|\mathbf{p}) &\propto \text{Gam}(\alpha_0|1, 1) * \text{Dir}\left(\mathbf{p}|\frac{\alpha_0}{J}, \dots, \frac{\alpha_0}{J}\right) \propto \exp(-\alpha_0) \frac{1}{B(\frac{\alpha_0}{J})} \prod_{j=1}^J p_j^{\frac{\alpha_0}{J}} \\ &\propto \exp(-\alpha_0) \frac{\Gamma(\alpha_0)}{[\Gamma(\frac{\alpha_0}{J})]^J} \prod_{j=1}^J p_j^{\frac{\alpha_0}{J}} * \mathbf{1}(\alpha_0 > 0). \end{aligned} \quad (7)$$

We obtain no closed-form distributions for both concentration parameters α and α_0 , hence we apply adaptive Metropolis-Hastings to obtain posterior samples. The log of the full condition in eq. (6) is:

$$\log \pi(\alpha|\mathbf{p}_{1:D}, \mathbf{p}) = -\alpha + D \log(\Gamma(\alpha)) + \sum_{d=1}^D \sum_{j=1}^J [\alpha p_j \log(p_{j,d}) - \log(\Gamma(\alpha p_j))] + \text{const.},$$

and in eq. (7) is:

$$\log \pi(\alpha_0|\mathbf{P}) = -\alpha_0 + \log(\Gamma(\alpha_0)) - J \log(\Gamma(\frac{\alpha_0}{J})) + \sum_{j=1}^J \frac{\alpha_0}{J} \log(p_j) + \text{const.}$$

A.5.1 Adaptive Metropolis-Hastings for α

1. Since α is always greater than zero, we apply the following transformation to map α to the real axis:

$$\alpha \in \mathbb{R}_+ \mapsto x \in \mathbb{R},$$

where $x = t(\alpha) = \log(\alpha)$.

2. We apply an adaptive random walk in the transformed space, where the variance of proposal is adapted in similar fashion to Appendix A.4.1, with the sample variance computed by sequentially updating the required statistics.

3. To compute the Jacobian of the transformation, we differentiate $t(\alpha)$ with respect to α :

$$\frac{dt(\alpha)}{d\alpha} = \frac{d \log(\alpha)}{d\alpha} = \frac{1}{\alpha}.$$

4. Hence the acceptance probability simplifies to:

$$\alpha(\alpha_{new}, \alpha_{old}) = \min\{1, \tilde{\alpha}(\alpha_{new}, \alpha_{old})\},$$

where

$$\tilde{\alpha}(\alpha_{new}, \alpha_{old}) = \log \left[\frac{\pi(\alpha_{new}) q_n(\alpha_{old}|\alpha_{new})}{\pi(\alpha_{old}) q_n(\alpha_{new}|\alpha_{old})} \right] = \log \left[\frac{\pi(\alpha_{new}) \alpha_{new}}{\pi(\alpha_{old}) \alpha_{old}} \right].$$

A.6 Unique Parameters

The full conditional distribution for μ^* and ϕ^* is:

$$\begin{aligned} \pi(\mu_j^*, \phi_j^* | \mathbf{Z}, \mathbf{b}, \alpha_\phi^2, \mathbf{Y}, \beta) &\propto \prod_{g=1}^G \log N(\mu_{j,g}^* | 0, \alpha_\mu^2) \log N(\phi_{j,g}^* | b_0 + b_1 \log(\mu_{j,g}^*), \alpha_\phi^2) \\ &\quad * \prod_{(c,d): z_{c,d}=j} \prod_{g=1}^G \text{NB}(y_{c,g,d} | \mu_{j,g}^* \beta_{c,d}, \phi_{j,g}^*). \end{aligned}$$

Since the genes are conditionally independent, we can write the full condition for $\mu_{j,g}^*$ and $\phi_{j,g}^*$ as:

$$\begin{aligned} \pi(\mu_{j,g}^*, \phi_{j,g}^* | \mathbf{Z}, \mathbf{b}, \alpha_\phi^2, \mathbf{Y}, \beta) &\propto \left(\frac{1}{\mu_{j,g}^* \phi_{j,g}^*} \right) \exp \left(-\frac{1}{2\alpha_\mu^2} (\ln \mu_{j,g}^*)^2 - \frac{1}{2\alpha_\phi^2} (\ln \phi_{j,g}^* - (b_0 + b_1 \log \mu_{j,g}^*))^2 \right) \\ &\quad * \prod_{(c,d): z_{c,d}=j} \binom{y_{c,g,d} + \phi_{j,g}^* - 1}{\phi_{j,g}^* - 1} \left(\frac{\phi_{j,g}^*}{\mu_{j,g}^* \beta_{c,d} + \phi_{j,g}^*} \right)^{\phi_{j,g}^*} \left(\frac{\mu_{j,g}^*}{\mu_{j,g}^* \beta_{c,d} + \phi_{j,g}^*} \right)^{y_{c,g,d}}. \end{aligned} \quad (8)$$

The full conditional distribution has no closed-form, hence we apply adaptive Metropolis-Hastings to obtain posterior samples. We first compute the log-likelihood of eq. (8):

$$\begin{aligned} \log \pi(\mu_{j,g}^*, \phi_{j,g}^* | \dots) &= -\log(\mu_{j,g}^* \phi_{j,g}^*) - \frac{1}{2\alpha_\mu^2} (\ln \mu_{j,g}^*)^2 - \frac{1}{2\alpha_\phi^2} (\ln \phi_{j,g}^* - (b_0 + b_1 \log \mu_{j,g}^*))^2 \\ &\quad + \sum_{(c,d): z_{c,d}=j} \log \binom{y_{c,g,d} + \phi_{j,g}^* - 1}{\phi_{j,g}^* - 1} + \phi_{j,g}^* \log \left(\frac{\phi_{j,g}^*}{\mu_{j,g}^* \beta_{c,d} + \phi_{j,g}^*} \right) + y_{c,g,d} \log \left(\frac{\mu_{j,g}^*}{\mu_{j,g}^* \beta_{c,d} + \phi_{j,g}^*} \right) + \text{const.} \end{aligned}$$

A.6.1 Adaptive Metropolis Hastings for μ and ϕ

1. Since (μ^*, ϕ^*) are always positive, we transform to the real axis:

$$(\mu^*, \phi^*) \in \mathbb{R}_+^2 \mapsto \mathbf{x} \in \mathbb{R}^2,$$

where $t_1(\mu^*, \phi^*) = x_1 = \log(\mu^*)$ and $t_2(\mu^*, \phi^*) = x_2 = \log(\phi^*)$.

2. We apply an adaptive random walk in the transformed space, where the covariance matrix of proposal is adapted in similar fashion to Appendix A.4.1, with the sample covariance matrix computed by sequentially updating the required statistics.
3. The Jacobian matrix of the transformation is:

$$J_{\mathbf{t}(\mu^*, \phi^*)} = \begin{pmatrix} \frac{dt_1}{d\mu^*} & \frac{dt_1}{d\phi^*} \\ \frac{dt_2}{d\mu^*} & \frac{dt_2}{d\phi^*} \end{pmatrix} = \begin{pmatrix} \frac{1}{\mu^*} & 0 \\ 0 & \frac{1}{\phi^*} \end{pmatrix};$$

and the log determinant of the Jacobian is:

$$\log \det J_{\mathbf{t}(\mu^*, \phi^*)} = \log \left[\frac{1}{\mu^* \phi^*} \right] = -\log(\mu^*) - \log(\phi^*).$$

4. The corresponding acceptance probability is given by:

$$\alpha((\mu^*, \phi^*)_{new}, (\mu^*, \phi^*)_{old}) = \min\{1, \exp[\tilde{\alpha}((\mu^*, \phi^*)_{new}, (\mu^*, \phi^*)_{old})]\},$$

where

$$\tilde{\alpha}((\mu^*, \phi^*)_{new}, (\mu^*, \phi^*)_{old}) = \log \left[\frac{\pi((\mu^*, \phi^*)_{new})}{\pi((\mu^*, \phi^*)_{old})} \right] - \log(\mu_{old}^*) - \log(\phi_{old}^*) + \log(\mu_{new}^*) - \log(\phi_{new}^*).$$

The above process is repeated for all unique parameters corresponding to occupied components. For non-occupied components, we can sample directly from the prior.

A.7 Capture Efficiencies

The full conditional distribution for β is:

$$\pi(\beta | \mathbf{Y}, \mathbf{Z}, \mu_{1:J}^*, \phi_{1:J}^*) \propto \prod_{j=1}^J \prod_{(c,d): z_{c,d}=j} \prod_{g=1}^G \text{NB}(y_{c,g,d} | \mu_{j,g}^* \beta_{c,d}, \phi_{j,g}^*) \prod_{d=1}^D \prod_{c=1}^{C_d} \text{Beta}(\beta_{c,d} | a_d^\beta, b_d^\beta).$$

Since all β are conditionally independent, they can be sampled in parallel, and we can write the full conditional distribution for cell c and gene g as:

$$\begin{aligned} \pi(\beta_{c,d} | \mathbf{Y}, \mathbf{Z}, \mu_{1:J}^*, \phi_{1:J}^*) &\propto \text{Beta}(\beta_{c,d} | a_d^\beta, b_d^\beta) \prod_{g=1}^G \text{NB}(y_{c,g,d} | \mu_{j,g}^* \beta_{c,d}, \phi_{j,g}^*) \\ &\propto \left[\prod_{g=1}^G \left(\frac{1}{\phi_{j,g}^* + \mu_{j,g}^* \beta_{c,d}} \right)^{\phi_{j,g}^* + y_{c,g,d}} (\beta_{c,d})^{y_{c,g,d}} \right] * (\beta_{c,d})^{a_d^\beta - 1} (1 - \beta_{c,d})^{b_d^\beta - 1} \mathbf{1}(\beta_{c,d} \in [0, 1]). \end{aligned}$$

As no closed-form is obtained, we apply adaptive Metropolis-Hastings to obtain posterior samples. First, the full-conditional on the log-scale is:

$$\begin{aligned} \log \pi(\beta_{c,d} | \dots) &= (a_d^\beta - 1) \log(\beta_{c,d}) + (b_d^\beta - 1) \log(1 - \beta_{c,d}) \\ &\quad - \sum_{g=1}^G (\phi_{j,g}^* + y_{c,g,d}) \log(\phi_{j,g}^* + \mu_{j,g}^* \beta_{c,d}) - y_{c,g,d} \log(\beta_{c,d}) + \text{const.} \end{aligned}$$

A.7.1 Adaptive Metropolis-Hastings for β

1. We apply a logit transformation to transform β into x , where x belongs to the real axis:

$$\beta \in [0, 1] \mapsto x \in \mathbb{R},$$

where $t(\beta) = \log\left(\frac{\beta}{1-\beta}\right) = x$.

2. We apply an adaptive random walk in the transformed space, where the variance of proposal is adapted in similar fashion to Appendix A.4.1, with the sample variance computed by sequentially updating the required statistics.

3. To Jacobian of the transformation is:

$$\frac{dt(\beta)}{d\beta} = \frac{d}{d\beta} (\log(\beta) - \log(1 - \beta)) = \frac{1}{\beta(1 - \beta)},$$

and the log of the determinant of the Jacobian is:

$$\log \left(\frac{1}{\beta(1 - \beta)} \right) = -\log(\beta) - \log(1 - \beta).$$

4. The acceptance probability is given by:

$$\alpha(\beta_{new}, \beta_{old}) = \min\{1, \exp[\tilde{\alpha}(\beta_{new}, \beta_{old})]\},$$

where

$$\tilde{\alpha}(\beta_{new}, \beta_{old}) = \log \left[\frac{\pi(\beta_{new})}{\pi(\beta_{old})} \right] + \log(\beta_{new}) + \log(1 - \beta_{new}) - \log(\beta_{old}) - \log(1 - \beta_{old}).$$

A.8 bayNorm Estimates of the Capture Efficiencies

In the bayNorm approach, capture efficiencies are estimated using the following approach:

$$\hat{\beta}_{c,d}^{\text{bay}} = \frac{\sum_{g=1}^G Y_{c,g,d}}{\frac{1}{C_d} \sum_{c=1, g=1}^{C_d, G} Y_{c,g,d}} \times \lambda,$$

where λ is the mean of estimated capture efficiencies. Under the default setting of bayNorm, $\lambda = 0.06$. The estimates are used to construct empirical priors for the capture efficiencies in our Norm-HDP model.

A.9 Marker Genes

Given the clustering allocation $\mathbf{Z} = (z_{c,d})_{c=1, d=1}^{C_d, D}$ of all cells across all datasets, we first focus on comparing the mean expression and dispersion across two clusters j and j' . We highlight that different dispersion parameters quantify changes in heterogeneity across cell subpopulations, while also accounting for the well-known mean-variance relationship in count data [Vallejos et al., 2016]. Web Figure A.1 depicts four scenarios for a single gene: on the top right, cells are differently expressed across the cell types with similar heterogeneity; on the bottom left, overall expression levels are similar but less stable with varying heterogeneity; and on the bottom right, cell types differ in both overall expression and heterogeneity.

To measure these changes, the posterior probability associated with the LFC decision rule is computed for each pair of clusters j and j' and each gene g . Specifically, let $P_g(j, j')$ and $L_g(j, j')$ be the posterior tail probabilities that the absolute LFC of the mean expression and dispersion between clusters j and j' is greater than the threshold τ_0 and ω_0 , respectively;

$$P_g(j, j') = \Pr \left(\left| \log \left(\frac{\mu_{j,g}^*}{\mu_{j',g}^*} \right) \right| > \tau_0 \mid \mathbf{Z}, \mathbf{Y} \right), \quad L_g(j, j') = \Pr \left(\left| \log \left(\frac{\phi_{j,g}^*}{\phi_{j',g}^*} \right) \right| > \omega_0 \mid \mathbf{Z}, \mathbf{Y} \right).$$

Global marker genes are identified by considering the maximum of the posterior tail probabilities across all pairs of clusters:

$$P_g^* = \max_{(j,j')} P_g(j, j'), \quad L_g^* = \max_{(j,j')} L_g(j, j').$$

Genes with high values of P_g^* or L_g^* have a high posterior probability that the LFC in the mean expression or dispersion is greater than a threshold across at least two clusters. Formally genes are classified as DE if the maximum probability, P_g^* , is greater than the threshold value α_M , and genes are classified as DD if the maximum probability, L_g^* , is greater than the threshold value α_D . By default, these threshold values (α_M, α_D) are set to control the expected false discovery rate (EFDR) to 5 percent [Vallejos et al., 2016]. In our context, these are given by:

$$\text{EFDR}_{\alpha_M}(\tau_0) = \frac{\sum_{g=1}^G (1 - P_g^*(\tau_0)) \mathbf{I}(P_g^*(\tau_0) > \alpha_M)}{\sum_{g=1}^G (1 - P_g^*(\tau_0))},$$

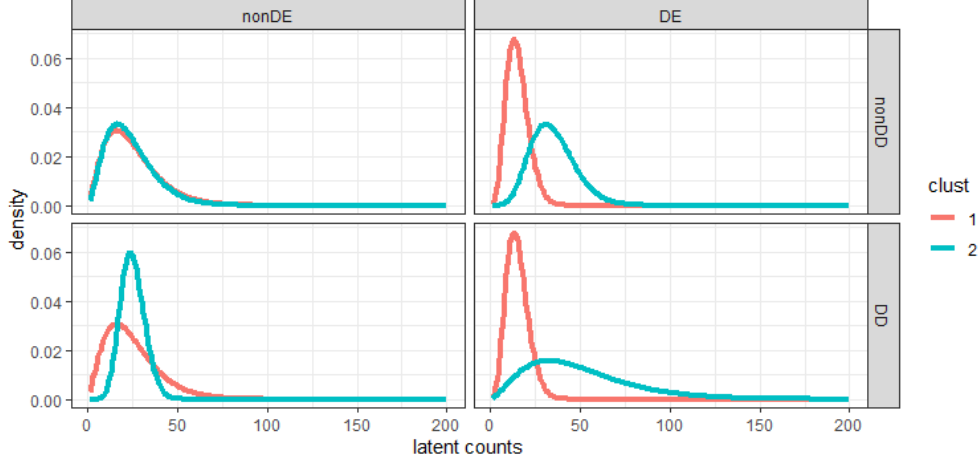
$$\text{EFDR}_{\alpha_D}(\omega_0) = \frac{\sum_{g=1}^G (1 - L_g^*(\omega_0)) \mathbf{I}(L_g^*(\omega_0) > \alpha_D)}{\sum_{g=1}^G (1 - L_g^*(\omega_0))}.$$

Global marker genes can be computed by conditioning on the clustering estimate to detect important genes that distinguish between the identified cell subpopulations. Alternatively, uncertainty in the clustering structure can also be incorporated by integrating the maximum probability P_g^* or L_g^* with respect to the posterior of \mathbf{Z} , which can be approximated by averaging P_g^* or L_g^* across the MCMC samples.

While global marker genes distinguish between at least two cell subtypes, one might also be interested in identifying local marker genes, or cluster-specific marker genes, with unique expression or dispersion for a specified cell-subtype j in comparison with all others. In this case, the minimum of the posterior tail probabilities is computed:

$$P_{g,j}^* = \min_{j' \neq j} P_g(j, j'), \quad L_{g,j}^* = \min_{j' \neq j} L_g(j, j').$$

For cluster j , genes with high values of $P_{g,j}^*$ or $L_{g,j}^*$ have a high posterior probability that the LFC in the mean expression or dispersion is greater than a threshold between cluster j and any other cluster. If the minimum posterior tail probability is greater than a threshold (calibrated through EFDR), the gene is detected as locally DE or DD for the specified cluster. Figure A.1 demonstrates the hypothetical density of latent counts for genes with different global characteristics.



Web Figure A.1: Density of hypothetical latent counts across the four combinations of non-DE/DE and non-DD/DD genes. For illustration, we have assumed a total of 2 clusters.

A.10 Latent Counts

Equation below shows the posterior mean of the latent count given the allocation variables, capture efficiencies and unique parameters.

$$\mathbb{E}[y_{c,g,d}^0 | y_{c,g,d}, z_{c,d} = j, \beta_{c,d}, \mu_j^*, \phi_j^*] = y_{c,g,d} \frac{\mu_{j,g}^* + \phi_{j,g}^*}{\mu_{j,g}^* \beta_{c,d} + \phi_{j,g}^*} + \mu_{j,g}^* \frac{\phi_{j,g}^* (1 - \beta_{c,d})}{\mu_{j,g}^* \beta_{c,d} + \phi_{j,g}^*},$$

and the posterior mean of the latent counts can be approximated by the MCMC average:

$$\mathbb{E}[y_{c,g,d}^0 | \mathbf{Y}] \approx \frac{1}{T} \sum_{t=1}^T \mathbb{E}[y_{c,g,d}^0 | y_{c,g,d}, z_{c,d}^{(t)} = j, \beta_{c,d}^{(t)}, \mu_j^{*(t)}, \phi_j^{*(t)}],$$

where $\mathbf{Y} = (\mathbf{Y}_1, \dots, \mathbf{Y}_D)$.

B Web Appendix B: Simulations

B.1 Simulation 1: Data Generation

In the first simulation, the two datasets are simulated using the following model:

$$\begin{aligned} y_{c,g,d} | z_{c,d} = j, \mu_{j,g}^*, \beta_{c,d}, \phi_{j,g}^* &\sim \text{NB}(\mu_{j,g}^* \beta_{c,d}, \phi_{j,g}^*), \\ z_{c,d} | (p_{1,d}^J, \dots, p_{J,d}^J) &\sim \text{Cat}(p_{1,d}^J, \dots, p_{J,d}^J), \\ \mu_{j,g}^* &\sim \log\text{N}(0, \alpha_\mu^2), \\ \phi_{j,g}^* | \mu_{j,g}^* &\sim \log\text{N}(b_0 + b_1 \log(\mu_{j,g}^*), \alpha_\phi^2), \\ \beta_{c,d} &\sim \text{Beta}(a_d^\beta, b_d^\beta), \end{aligned}$$

where we set $b_1 = 0; b_2 = 3; \alpha_\mu^2 = 1; \alpha_\phi^2 = 1$ and $a_d^\beta = 1; b_d^\beta = 0.5$ for both datasets. The first dataset contains $C_1 = 50$ cells and the second contains $C_2 = 100$ cells, with $G = 50$ genes. We assume there are $J = 3$ clusters, with true cell proportions $(p_{1,1}, p_{2,1}, p_{3,1}) = (0.6, 0.4, 0)$ for dataset 1 and $(p_{1,2}, p_{2,2}, p_{3,2}) = (0.4, 0, 0.6)$ for dataset 2.

B.2 Simulation 2: Data Generation

In the second simulation, we assume a non-linear relationship between the mean expressions and dispersions, to assess robustness to misspecification. The two datasets are generated as in Simulation 1 (Appendix B.1), however, we assume

the following relationship:

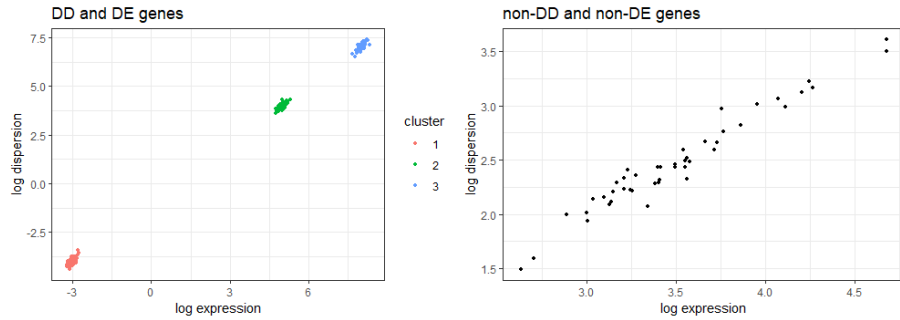
$$\phi_{j,g}^* | \mu_{j,g}^* \sim \text{logN}(4 - 2/\mu_{j,g}, \alpha_\phi^2),$$

and values of α_μ^2 ; α_ϕ^2 ; a_d^β and b_d^β are set to be the same as in Simulation 1.

B.3 Simulation 3: Data Generation

In Simulation 3, we test the ability of our algorithm to detect global differentially expressed and dispersed genes. In this case, we have $G = 150$ genes; $C_1 = 300$ cells in dataset 1 and $C_2 = 400$ cells in dataset 2. We assume that there are $J = 3$ clusters, with dataset-specific allocation proportions $(0.8, 0.2, 0)$ and $(0.8, 0, 0.2)$ for dataset 1 and 2, respectively. For simplicity, we assume the first 70 percent of the genes are DD and DE, specifically, these are the genes with indices 1 to 105.

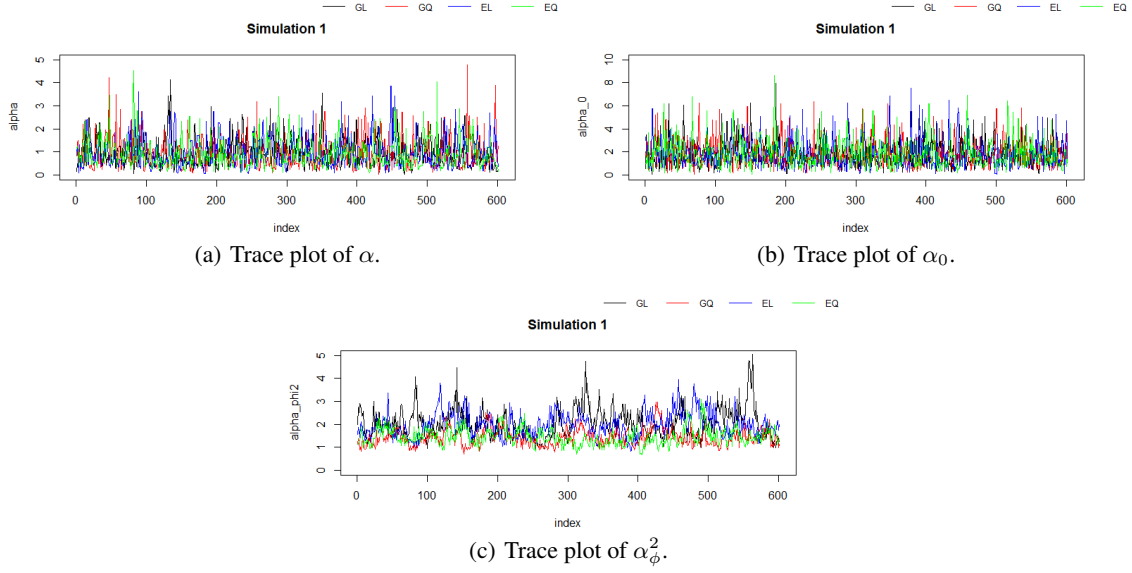
Based on the results from the real data, non-DE genes tend to be highly expressed. Thus, we set the true mean for non-DE genes $\mu_{j,g}^*$ to μ_g^* , with $\mu_g^* \sim \text{logN}(3.5, 0.5)$. Instead, for DE genes, we set the true mean $\mu_{j,g}^* \sim \text{logN}(m_j, 0.1)$, where $m_{1:J} = (-3, 5, 8)$. We assume all DE genes are also DD and vice versa. For non-DD (and non-DE) genes, we set the true dispersion $\phi_{j,g}^* = \phi_g^*$ with $\phi_g^* \sim \text{logN}(b_0 + b_1 \log(\mu_g^*), 0.1)$, where $b_0 = -1$ and $b_1 = 1$. For DD (and DE) genes, we set the true dispersion $\phi_{j,g}^* \sim \text{logN}(b_0 + b_1 \log(\mu_{j,g}^*), 0.1)$. The true relationships between mean expressions and dispersions are shown in Web Figure B.2.



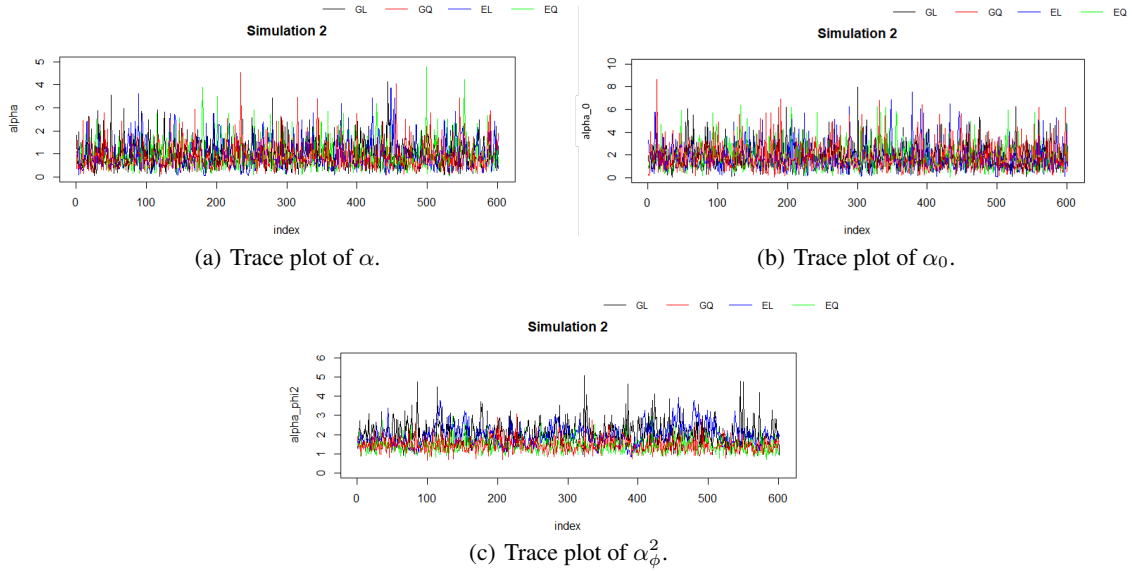
Web Figure B.2: True mean-dispersion relationships for DE and DD genes (left) and non-DE (also non-DD) genes (right). On the left, different colors are used to represent mean expressions and dispersions from different clusters.

B.4 Simulations 1 and 2: Results

Traceplots of concentration parameters and α_ϕ^2 for Simulation 1 and Simulation 2 provided in Web Figures B.3 and B.4 suggest convergence:

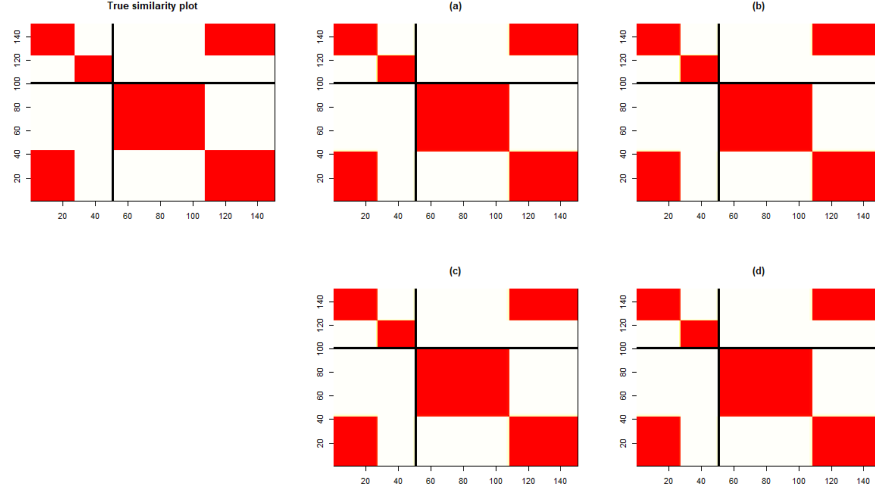


Web Figure B.3: Traceplots of the concentration parameters and regression parameter α_ϕ^2 for Simulation 1. Colors represent the chains under the different prior and model choices.

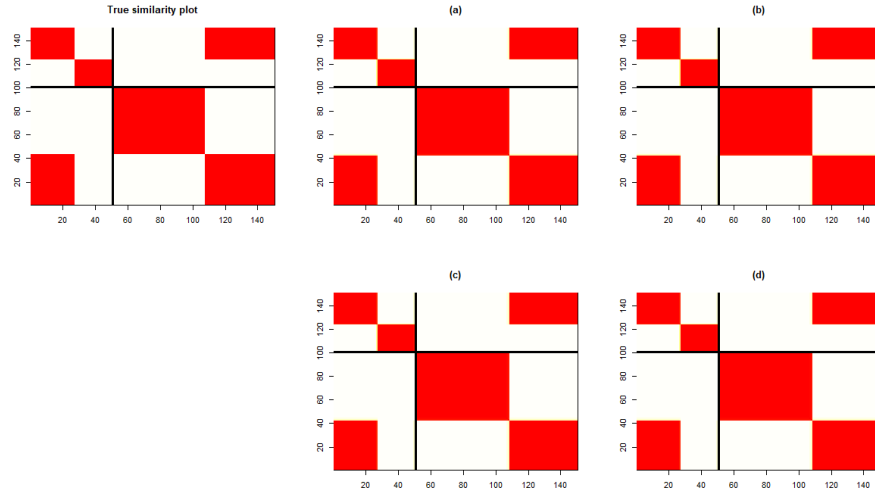


Web Figure B.4: Traceplots of the concentration parameters and regression parameter α_ϕ^2 for Simulation 2. Colors represent the chains under the different prior and model choices.

In Web Figure B.5 and B.6, we compare the true similarity matrix with the posterior similarity matrix obtained from the different prior (general vs. empirical) and model (linear vs. quadratic) choices, for Simulation 1 and 2 respectively. In all cases, the results highlight that the true clustering structure is well recovered.

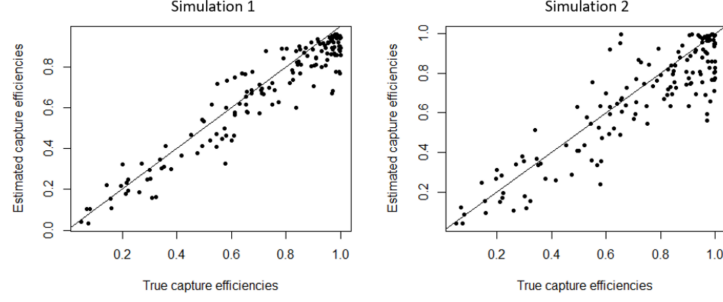


Web Figure B.5: Comparison of the true and posterior similarity matrix for Simulation 1, with the true similarity matrix (left) and the posterior similar matrix with (a) the linear model and general prior, (b) the linear model and empirical prior, (c) the quadratic model and general prior, and (d) the quadratic model and empirical prior.



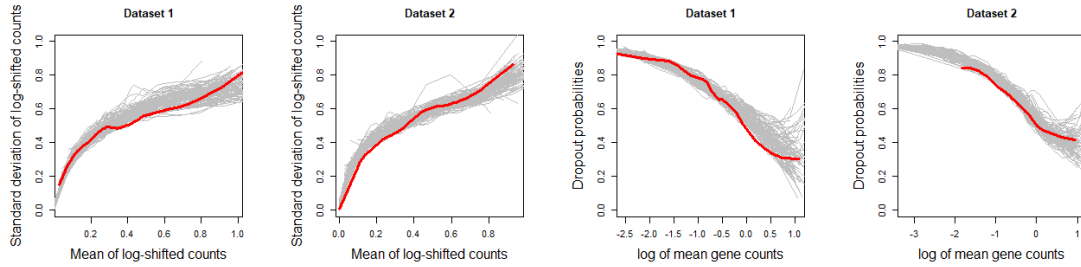
Web Figure B.6: Comparison of the true and posterior similarity matrix for Simulation 2, with the true similarity matrix (left) and the posterior similar matrix with (a) the linear model and general prior, (b) the linear model and empirical prior, (c) the quadratic model and general prior, and (d) the quadratic model and empirical prior.

Web Figure B.7 compares the true capture efficiencies with estimated capture efficiencies for Simulation 1 and Simulation 2, respectively. The figures highlight that the informative prior choice helps to mitigate indentifiability issues.

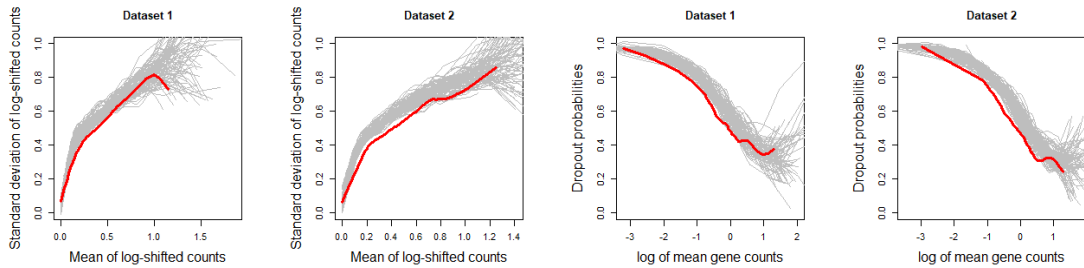


Web Figure B.7: Comparison between the true capture efficiencies and the posterior mean of capture efficiencies for Simulation 1 (left) and Simulation 2 (right).

Posterior predictive checks are performed to assess the fit of the model. We compare the mean of log-shifted counts against the standard deviation of the log-shifted counts as well as the log of the mean counts against the empirical dropout probabilities, computed across cells for each gene. Web Figure B.8 compares fitted relationship for each replicated dataset (in grey) with the fitted relationship for observed data (in red), for both simulations.



(a) Posterior predictive checks for Simulation 1



(b) Posterior predictive checks for Simulation 2

Web Figure B.8: Posterior predictive checks for (a) Simulation 1 and (b) Simulation 2. Grey and red lines are the fitted relationships for the replicated and simulated datasets, respectively. The left two columns are for the relationship between the mean and standard deviation of the log shifted counts. The last two columns are for the relationship between the log of the mean counts and dropout probabilities.

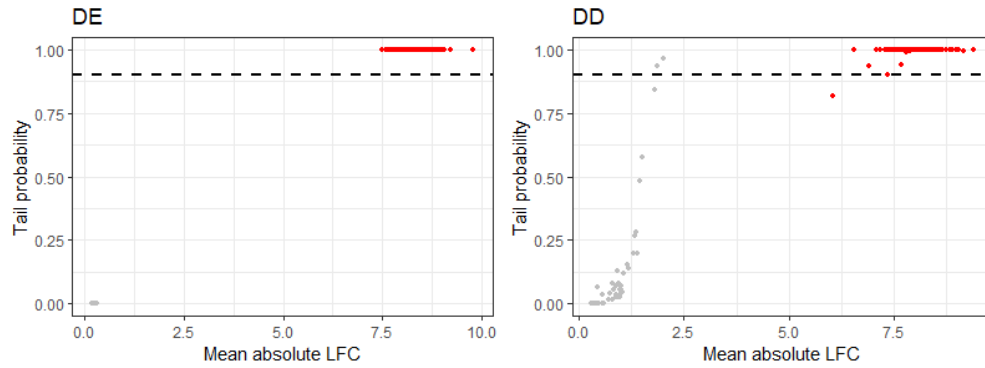
Table B.1 compares the recover of true parameters between several clustering methods and model settings.

Web Table B.1: Comparison of the different clustering solutions based on the VI and ARI to measure distance between the true and estimated clustering. Simulation 1: true relationship between unique parameters is linear. Simulation 2: true relationship between unique parameters is monotonically increasing, but non-linear and non-quadratic.

	General		Empirical		Seurat	CIDR	TSCAN
	Linear	Quadratic	Linear	Quadratic			
Simulation 1 - VI	0.00	0.00	0.00	0.00	0.31	1.30	0.58
Simulation 2 - VI	0.00	0.00	0.00	0.00	0.31	1.38	0.75
Simulation 1 - ARI	1.00	1.00	1.00	1.00	0.87	0.28	0.72
Simulation 2 - ARI	1.00	1.00	1.00	1.00	0.87	0.26	0.63

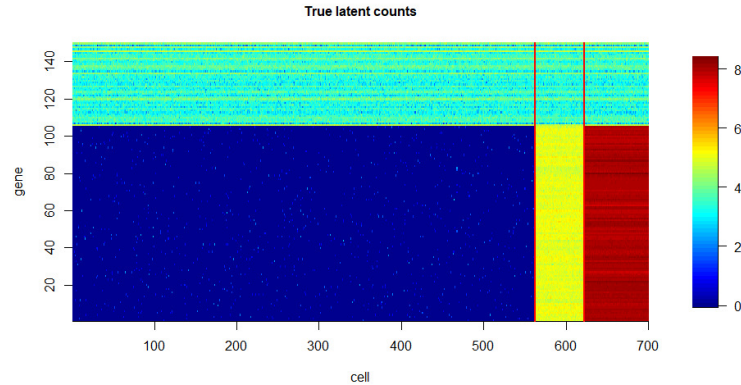
B.5 Simulation 3: Results

Web Figure B.9 shows the posterior estimated relationship between mean absolute log-fold change and tail probabilities corresponding to both mean expressions and dispersions.

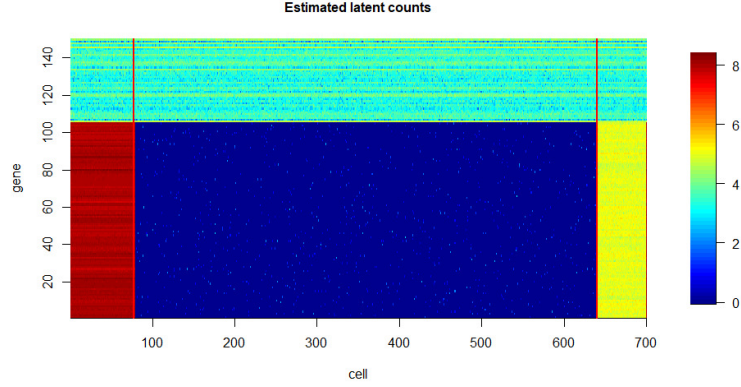


Web Figure B.9: Relationship between the mean absolute LFC and tail probability. The horizontal dashed lines represent the threshold for classifying DE and DD; all genes with tail probabilities greater than this threshold are classified as DE or DD. True DE or DD genes are represented in red and true non-DE or non-DD genes are represented in grey.

The true latent counts and the posterior estimated latent counts are illustrated in Web Figures B.10 and B.11, respectively, for Simulation 3. A comparison of the figures demonstrates that the latent counts are well recovered.



Web Figure B.10: Heat map of true latent gene-counts, with rows representing genes and columns representing cells. Cells are reordered by the true clustering, with cells from different clusters separated by vertical lines.



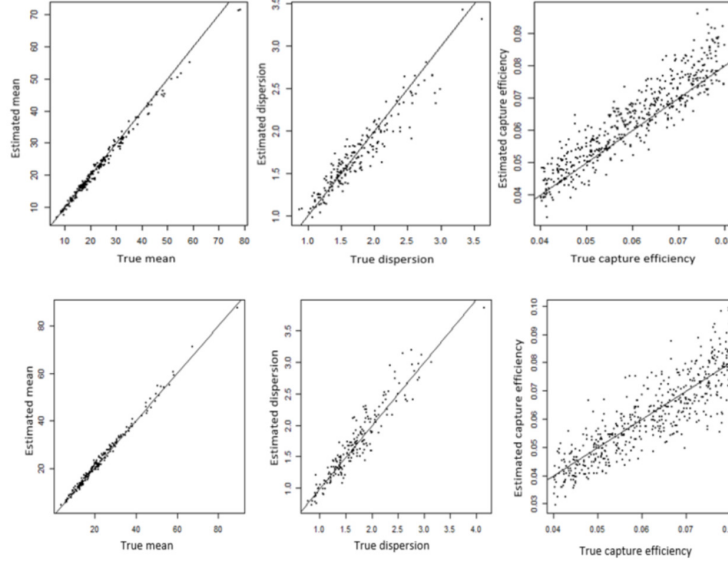
Web Figure B.11: Heat map of posterior estimated latent gene-counts, with rows representing genes and columns representing cells. Cells are reordered by the posterior estimated clustering, with cells from different clusters separated by vertical lines.

B.6 Additional Simulations with Misspecified Mean Capture Efficiencies

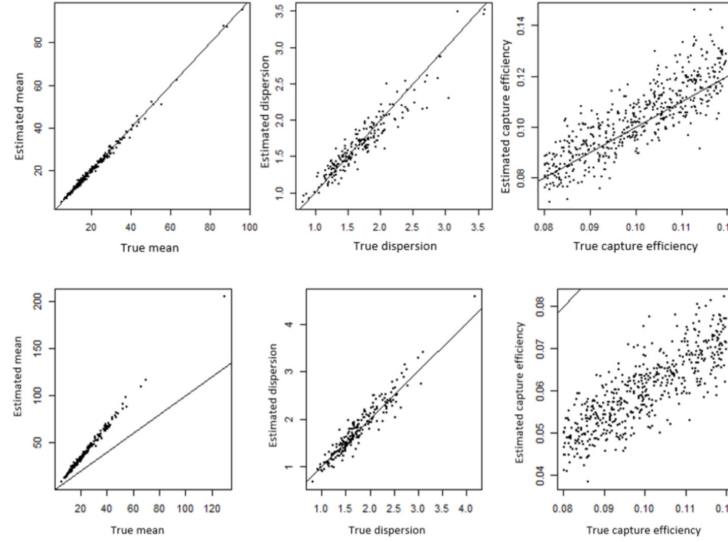
In the previous simulations, we used an informative prior for the capture efficiencies to mitigate identifiability issues. In addition, we carried out further simulations to investigate the effect of misspecification of the mean capture efficiency in our informative prior. Specifically, we set the true mean capture efficiency for dataset 1 and 2 as 0.06 and 0.10, respectively, and simulate the true unique parameters and capture efficiencies under the following model:

$$\begin{aligned}\beta_{c,1} &\sim \text{Unif}(0.04, 0.08), \\ \beta_{c,2} &\sim \text{Unif}(0.08, 0.12), \\ \phi_g &\sim \log\text{N}(3, 0.5), \\ \mu_g &\sim \log\text{N}(-1 + 0.5 \log(\phi_g), 0.1).\end{aligned}$$

We compare the *bayNorm* estimates of the capture efficiencies and unique parameters with our empirical Bayesian approach. Results for dataset 1 and 2 are shown in Web Figure B.12 and B.13, respectively. In the first dataset, the mean capture efficiency is correctly specified and both approaches are able to recover the true mean expression, dispersion, and capture efficiencies (Web Figure B.12). However, in the second dataset, the mean capture efficiency is misspecified; while *bayNorm* underestimates the capture efficiencies and overestimates the mean expressions, our empirical Bayesian approach is more robust to such minor misspecifications.



Web Figure B.12: Comparison between our Bayesian approach (top row) and *bayNorm* (bottom row) in recovering the mean-expression, dispersion and capture efficiency (left to right) for dataset 1.



Web Figure B.13: Comparison between our Bayesian approach (top row) and *bayNorm* (bottom row) in recovering the mean-expression, dispersion and capture efficiency (left to right) for dataset 2.

C Web Appendix C: PAX6 Data Analysis

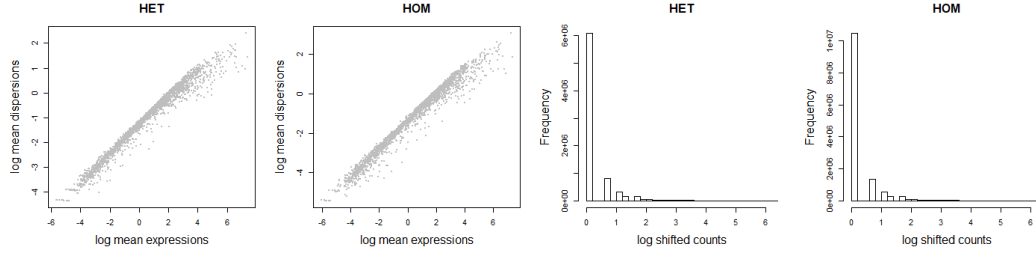
C.1 Filtering Process

For each dataset, we apply the following filters to select cells and genes:

1. Genes that are expressed by less than 5 cells are excluded (threshold chosen to remove half of the genes).
2. Cells with less than 2000 expressed genes are excluded (threshold chosen to remove cells with gene expressions less than 1.5 standard deviations below the empirical mean).
3. Cells with greater than 3.7 percent mitochondrial counts are excluded (threshold chosen to remove cells with mitochondrial counts greater than 1.5 standard deviations above the empirical mean).

4. Cells with gene counts greater than 17500 are excluded (threshold chosen to remove cells with gene counts greater than 1.5 standard deviations above than the empirical mean).
5. 2000 genes with the greatest variability are selected.

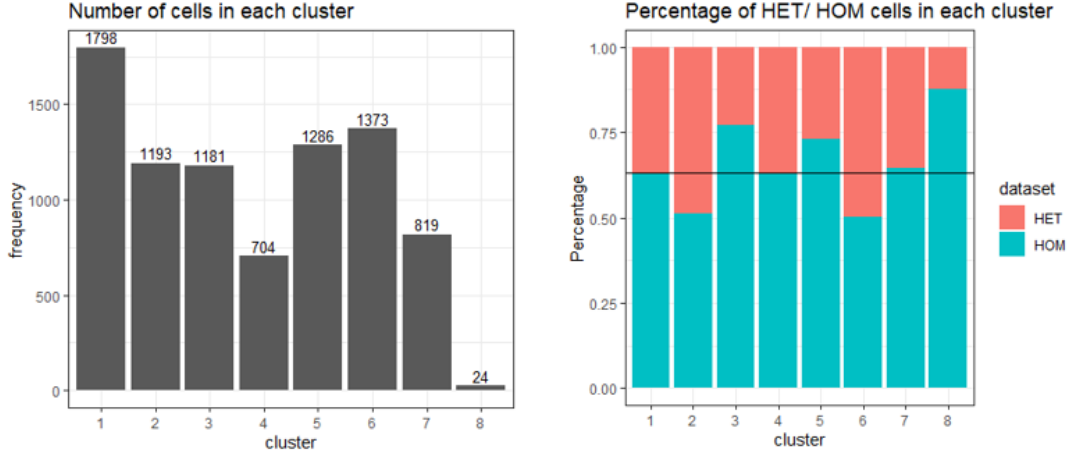
Finally, we use the union of genes remaining after applying all above filters to each dataset to form the final processed data. Note that all the ‘important’ genes are also included for each dataset (Web Table D.6). The empirical relationship between *bayNorm* estimates of the mean expressions and dispersions and the distribution of log shifted counts based on the final processed data are shown in Web Figure C.14.



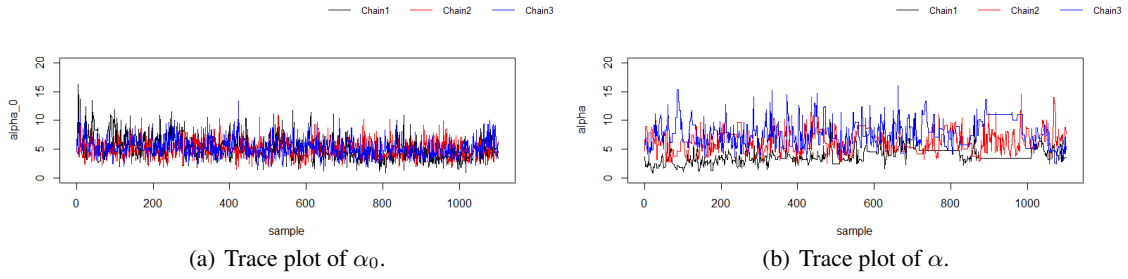
Web Figure C.14: Left two plots: empirical relationship between the log mean expressions and log dispersions. Right two plots: histogram of shifted latent gene-counts.

C.2 Results

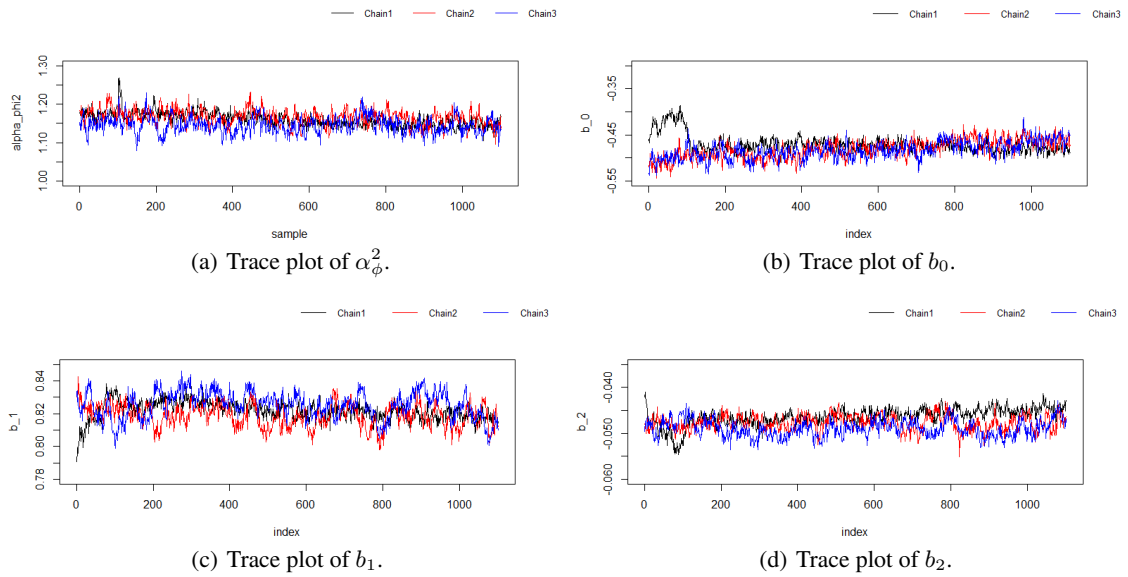
For the posterior estimate of clustering, we show the number of genes in each cluster and the proportion of HET/HOM genes in each cluster in Web Figure C.15. The traceplots of concentration parameters and hyperparameters are shown in Web Figures C.16 and C.17, respectively, suggest convergence. The posterior and prior distributions of these parameters are compared in Web Figures C.18 and C.19, highlighting the influence of the data. The relationship between the posterior estimated mean expressions and dispersions on the log-scale for each cluster are shown in Web Figure C.20; the relationships are similar across clusters. In addition, we compare the posterior estimated latent counts of two selected genes, namely ‘Fabp5’ and ‘H2afz’ across different clusters in Web Figure C.21. For gene ‘Fabp5’, there are no evident differences between the estimated latent counts across clusters, whereas for gene ‘H2afz’, differences across clusters are more apparent. Within each cluster, we observe greater variability of posterior estimated latent counts across cells for ‘H2afz’. For the capture efficiencies, we compare the *bayNorm* estimates and NormHDP posterior mean estimates of the capture efficiencies in Web Figure C.22 and present boxplots of the posterior mean capture efficiencies for cells in each cluster in Web Figure C.23. We observe that *bayNorm* tends to produce slightly larger estimates of the capture efficiencies compared with our model (Web Figure C.22). In addition, when comparing across clusters (Web Figure C.23), there is no evident difference, with the exception of the small group of cells in cluster 8, which are mostly from the mutant group and have higher capture efficiencies. Another important aspect of our model is the quantification of uncertainty in the estimated latent counts; we show for two gene ‘Ccnd2’ and ‘Tmsb4x’ the range of uncertainty in the posterior estimated latent counts in Web Figures C.24 and C.25.



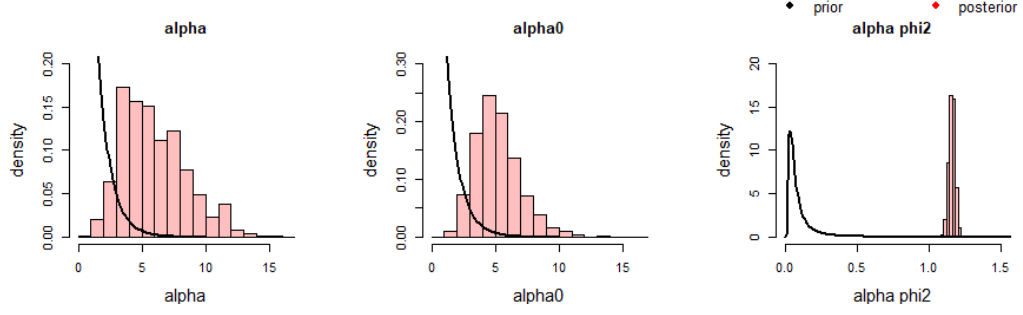
Web Figure C.15: Left: the number of cells within each cluster. Right: proportion of HET and HOM cells within each cluster, the horizontal line indicates the overall proportion of HOM cells across both datasets.



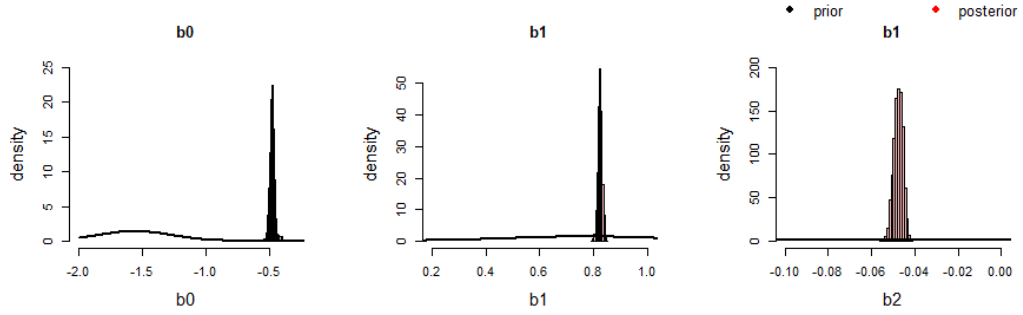
Web Figure C.16: Traceplot of concentration parameters.



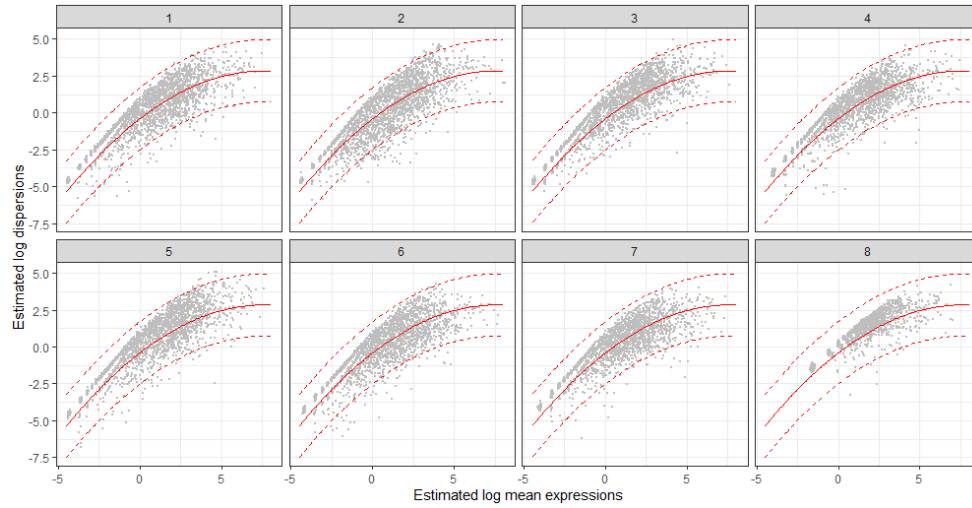
Web Figure C.17: Traceplot of regression parameters.



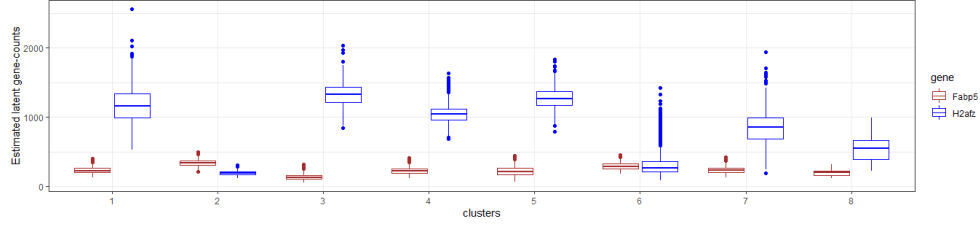
Web Figure C.18: Comparison between prior and posterior of α , α_0 and α_ϕ^2 (left to right). Prior densities are shown with black lines and posterior densities are shown with histograms.



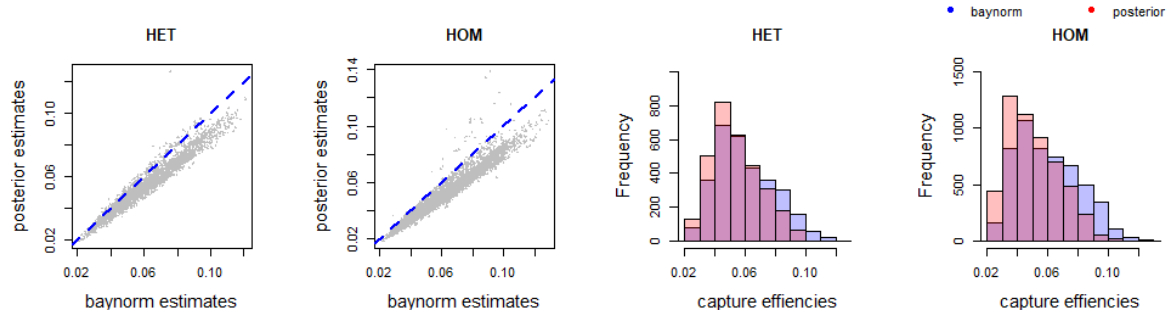
Web Figure C.19: Comparison between priors and posteriors of b_0 , b_1 and b_2 (left to right). Prior densities are shown with black lines and posterior densities are shown with histograms.



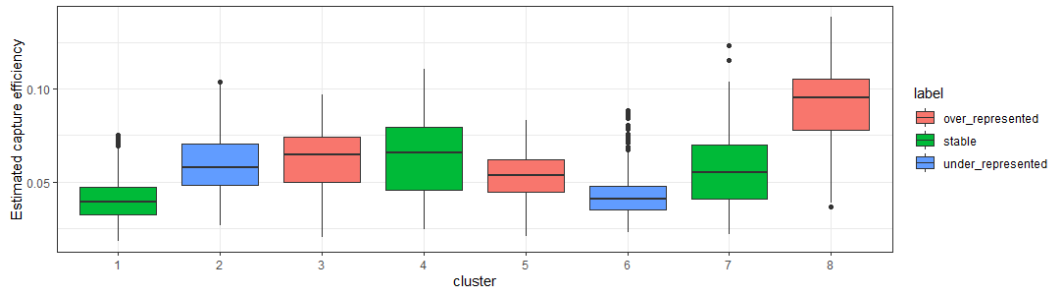
Web Figure C.20: Posterior estimated relationships between the mean expressions and dispersions for each cluster. The posterior means of the mean expressions and dispersions are plotted. The red dashed lines are the lower and upper bound of the 95 percent credible band obtained by considering posterior estimates of regression parameters b and α_ϕ^2 . The red solid line is the posterior estimated relationship.



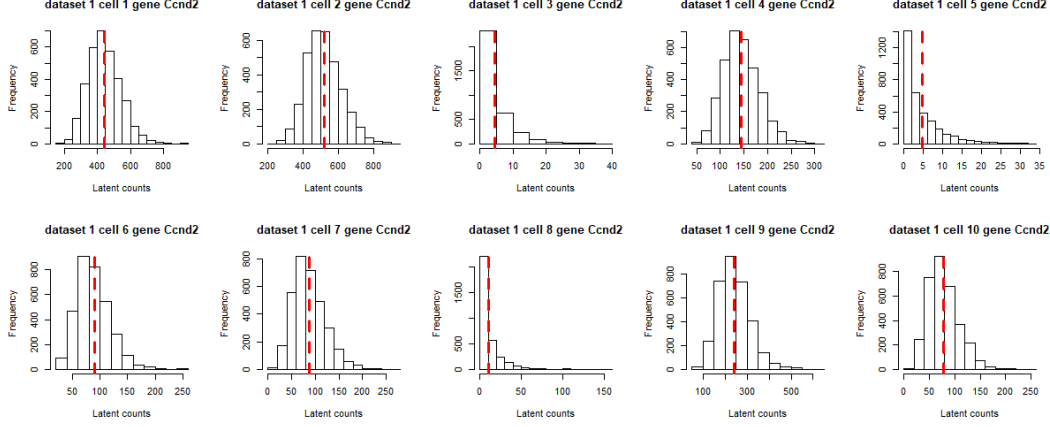
Web Figure C.21: Boxplots of posterior estimated latent counts across cells for genes Fabp5 and H2afz.



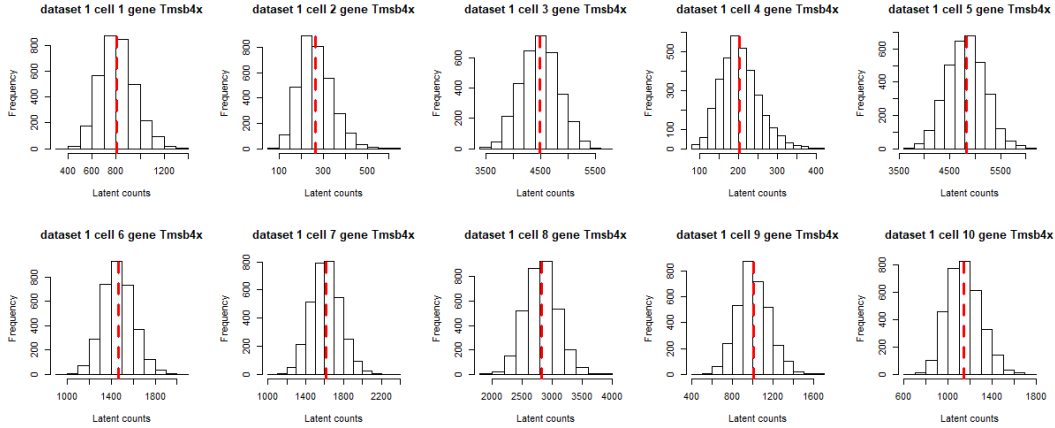
Web Figure C.22: Comparison of the bayNorm and posterior mean of the capture efficiencies. For the left two plots: bayNorm estimates are plotted against posterior estimates, and the dashed lines represents when the two values are equivalent. For the right two plots: histograms are drawn to compare distribution of the posterior mean capture efficiencies, with the baynorm and posterior estimates in blue and red, respectively.



Web Figure C.23: box plots of the estimated capture efficiencies for cells in each cluster. Capture efficiencies for cells in cluster 8 are much higher than cells from other clusters in general. Note that cluster 8 only has 24 allocated cells, mostly from HOM.



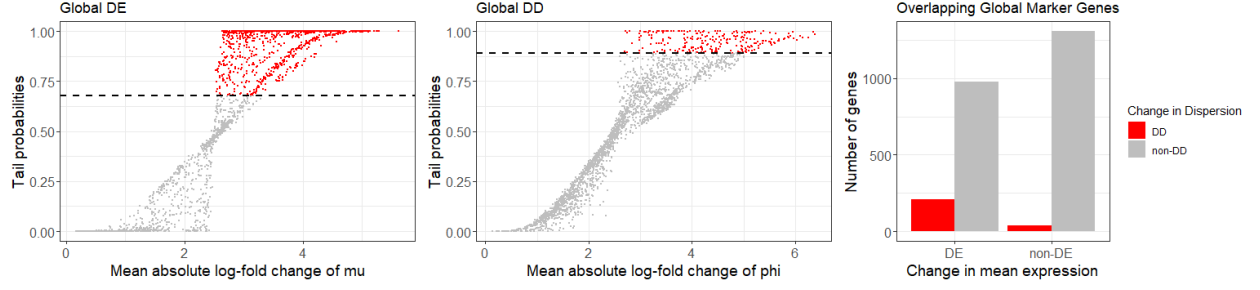
Web Figure C.24: Histograms of the posterior estimated latent counts for cell 1 to 10 for gene 'Ccnd2' in dataset 1. For each MCMC iteration, we compute the mean estimated latent count. The red vertical line indicates the overall mean latent count, averaged across all MCMC iterations, for a given gene and cell.



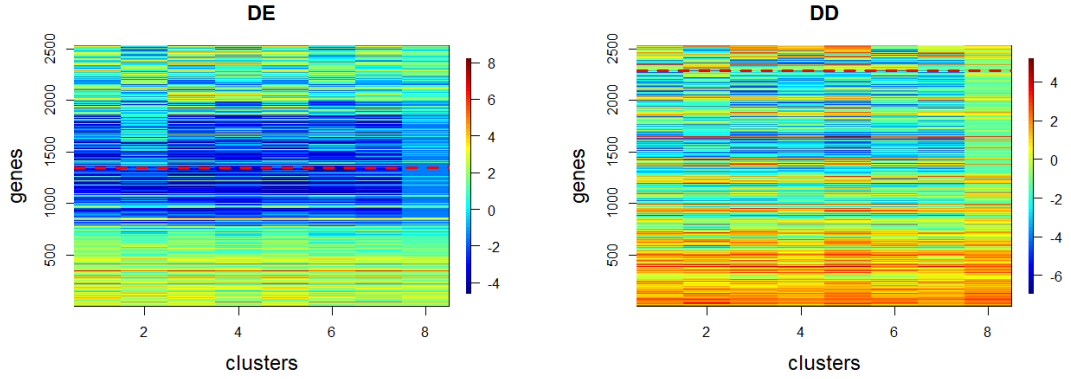
Web Figure C.25: Histograms of the posterior estimated latent counts for cell 1 to 10 for gene 'Tmsb4x' in dataset 1. For each MCMC iteration, we compute the mean estimated latent count. The red vertical line indicates the overall mean latent count, averaged across all MCMC iterations, for a given gene and cell.

C.3 Global Marker Genes

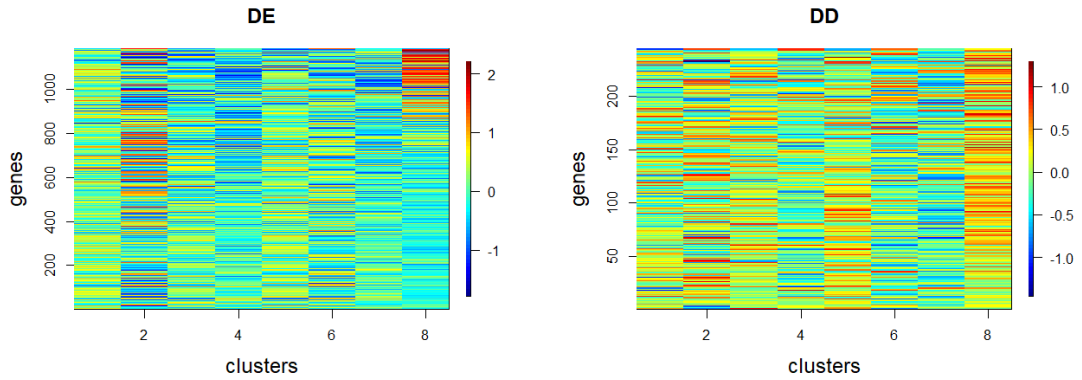
We first show the posterior relationship between absolute log-fold change and tail probabilities for global marker and non-marker genes in Web Figure C.26. In addition, we use heatmaps to observe differences in posterior estimated unique parameters between marker and non-marker genes in Web Figure C.27 and C.28. Further, we show that the posterior estimated mean expressions tend to be lower for global DE genes in comparison to the non-DE genes for each cluster (Web Figure C.29). However, overall, the posterior estimated dispersions are similar between DD and non-DD genes for each cluster (Web Figure C.30). In addition, we compare the posterior of the mean expression and dispersion within cluster for some global marker genes that are identified as DE or DD in Web Figure C.31. Further, heatmaps of the observed gene-counts with genes reordered by tail probabilities are presented in Web Figure C.32 and C.33 for DE and DD, respectively; genes above the horizontal red line are identified as global markers. t-SNE plots with only the global marker genes are shown in Web Figure C.34 for both the observed and posterior estimated latent counts; separation between clusters is more evident in the t-SNE plot based on the latent counts.



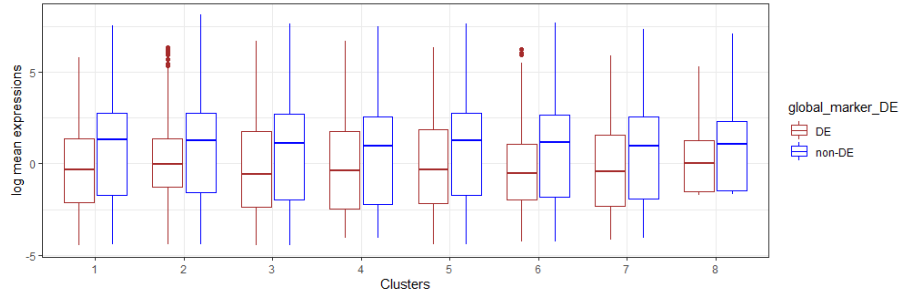
Web Figure C.26: Plots to show relationships between mean absolute LFCs and tail probabilities, and to summarise the number of genes with multiple global features



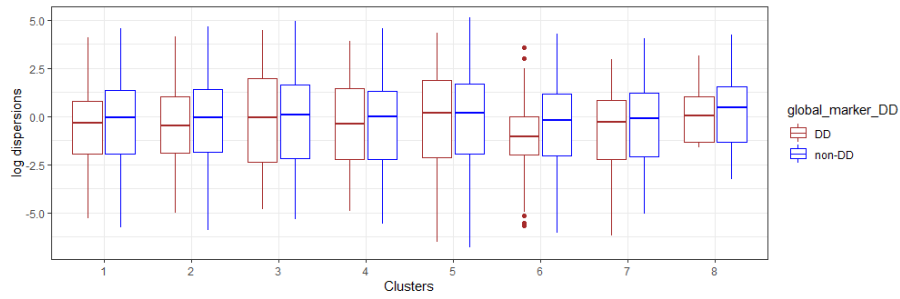
Web Figure C.27: Heat-maps of estimated unique parameters (mean expression on the left and dispersion on the right) on the log scale, with columns representing clusters and rows representing genes. Genes are reordered by tail probabilities; tail probabilities decrease as we move down the rows, with the horizontal dashed lines separating global marker genes from non-marker genes.



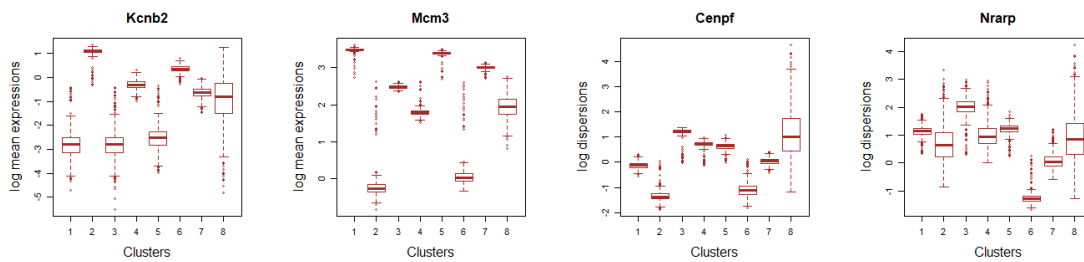
Web Figure C.28: Heat-maps of estimated relative unique parameters on the log-scale, with columns representing clusters and rows representing genes. Only global marker genes are included in the heat-maps. The relative value is defined as the estimated value minus the average across all clusters for that gene.



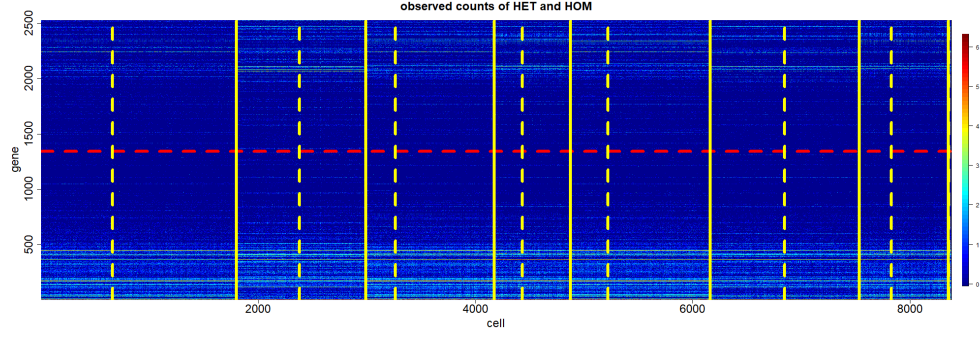
Web Figure C.29: Comparison of the posterior estimated log mean expressions between global DE and non-DE genes for each cluster.



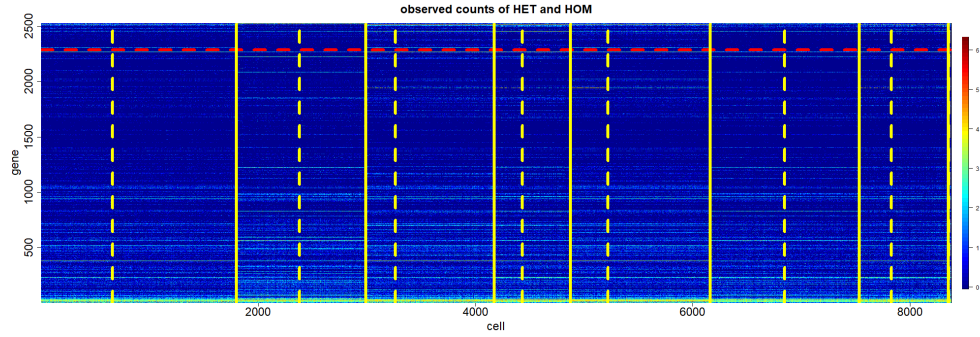
Web Figure C.30: Comparison of the posterior estimated log dispersions between global DD and non-DD genes for each cluster.



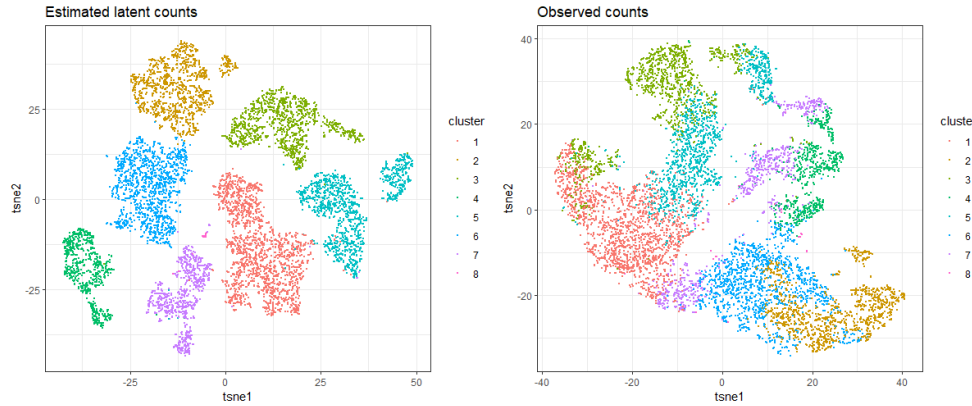
Web Figure C.31: Posterior of the unique parameters of global marker genes. Kcnc2 and Mcm3 are examples of global DE genes. Cenpf and Nrarp are examples of global DD genes.



Web Figure C.32: Heat-map of the observed counts for HET and HOM data. Cells from different clusters are separated by yellow vertical lines. Cells from different datasets are separated by yellow dashed lines. DE and non-DE genes are separated by the horizontal line such that genes above the horizontal line are global marker genes.



Web Figure C.33: Heat-map of observed counts for HET and HOM data. Cells from different clusters are separated by yellow vertical lines. Cells from different datasets are separated by yellow dashed lines. DD and non-DD genes are separated by the horizontal line such that genes above the horizontal line are global marker genes.



Web Figure C.34: t-SNE plot based on the estimated latent counts (left) and the observed counts (right) with global marker genes only. Cells are colored by cluster membership.

Web Table C.2: Top 20 Global DE genes

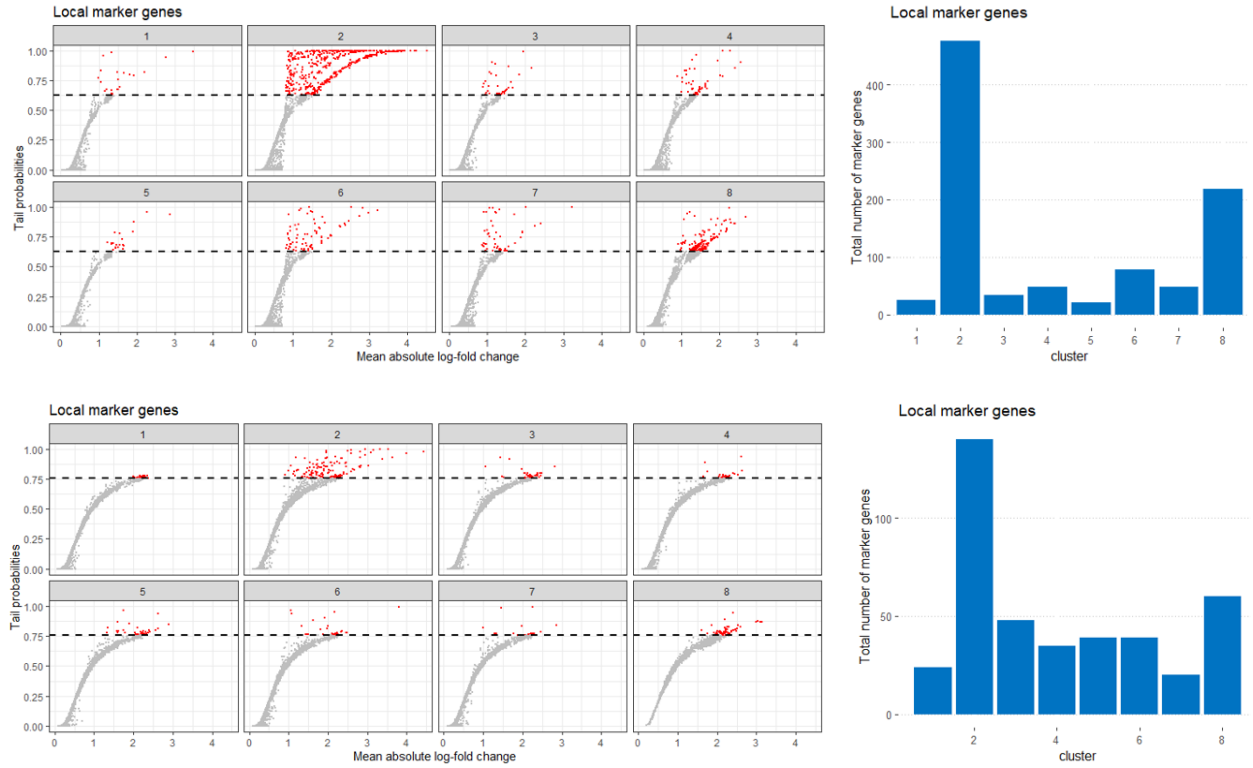
Lhx1	Fam196a	A2ml1	Cacna1e	Tbata	Neurod4	Kctd4	Serpinb2	C1ql3	Sln
Cemip	Zfp804a	Ppp2r2c	Nos1	6530403H02Rik	Gla2	Uncx	Pdzph1	S1pr1	Rbfox1

Web Table C.3: Top 20 Global DD genes

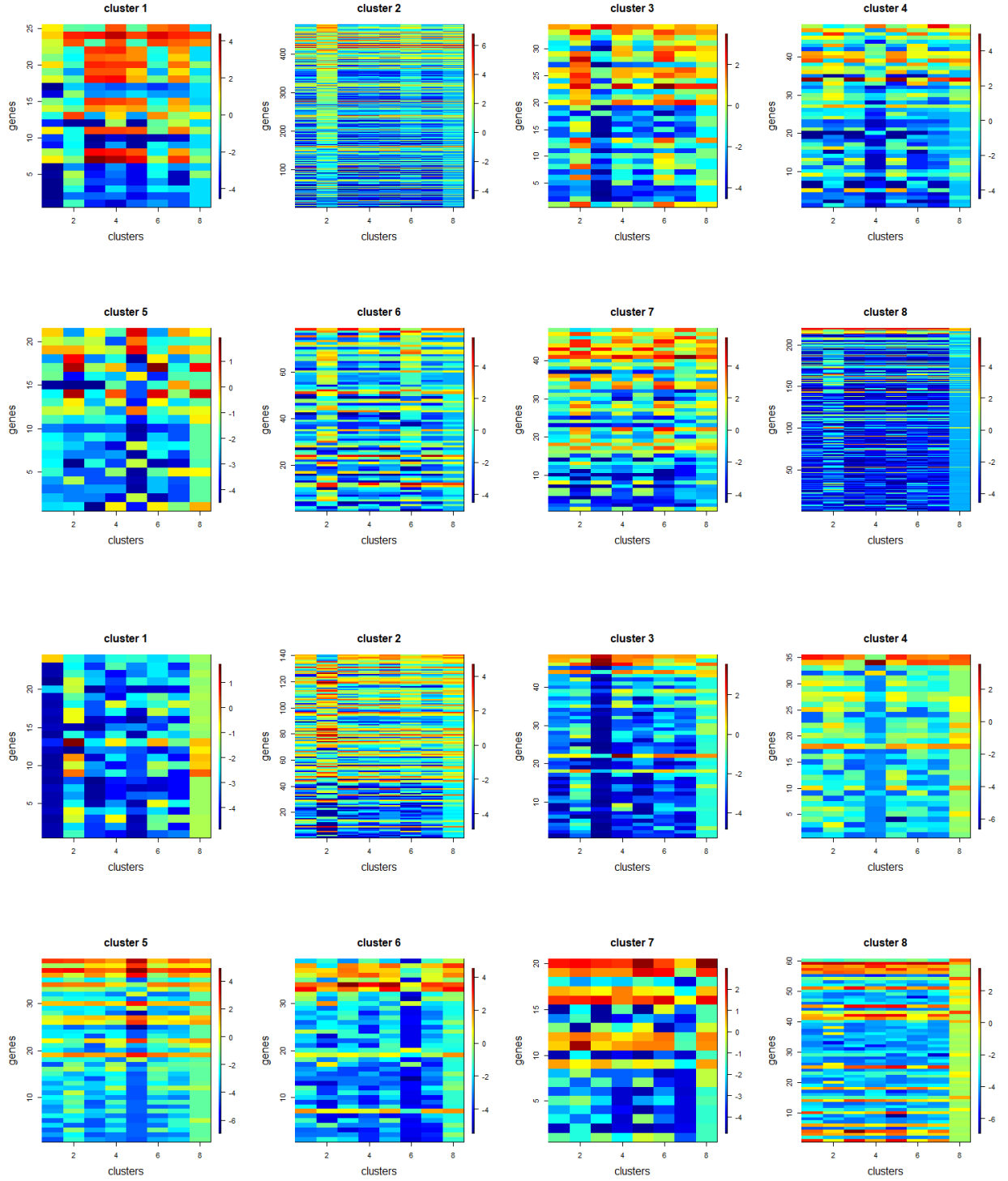
Cav2	Tnfrsf8	Etv1	Fkbp9	Sulf2	Cenpw	Zic5	Plk4	Nrp1	Racgap1
Tpbg	Cdca8	Cks1b	Dmrta2	Emx2	Birc5	Sox9	Nt5dc2	Cdca3	Tpx2

C.4 Local Marker Genes

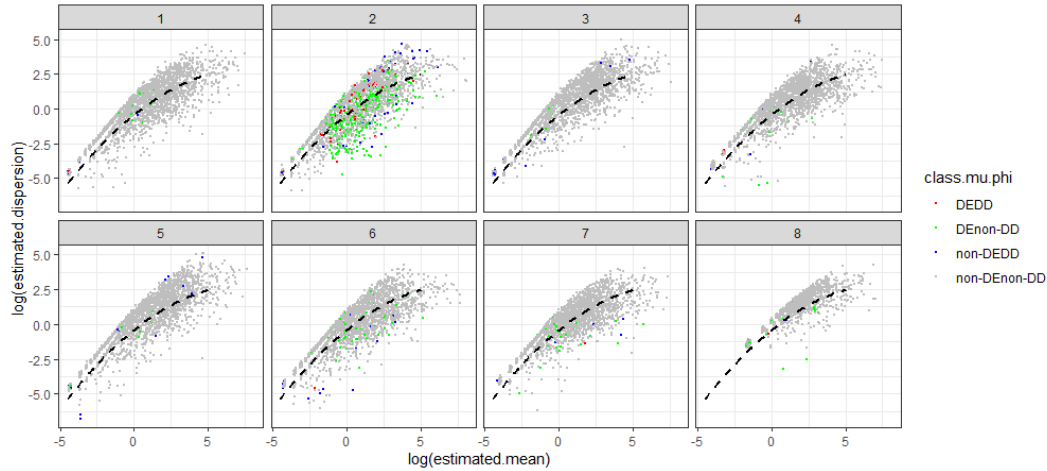
We present the relationships between absolute log-fold change and tail probabilities corresponding to local DE and local DD are shown in Web Figure C.35. In addition, bar charts to summarize the total number of local marker genes are also shown in Web Figure C.35. Heatmaps to compare estimated unique parameters of local marker genes for each cluster are shown in Web Figure C.36. Further, we present the relationship between the mean expressions and dispersions and highlight the local marker genes for each cluster in Web Figure C.37. No clear pattern is observed between the local features of the genes and the relationship between the unique parameters. In addition, we compare the estimated unique parameters between local marker and non-marker genes for each cluster; differences in the posterior estimated unique parameters are evident for local marker genes in 7 out of 8 clusters (Web Figure C.38 and C.39).



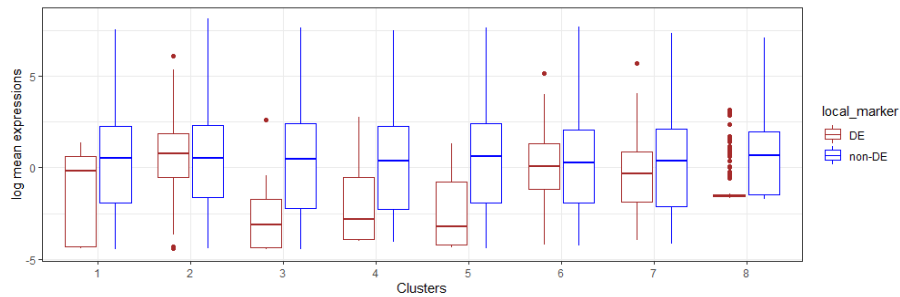
Web Figure C.35: Detection of local marker genes in terms of mean expressions (top row) and dispersions (bottom row). Left column: plots of tail probabilities against mean absolute LFCs for each cluster. Right column: a summary of the number of local DE (top) and DD genes (bottom).



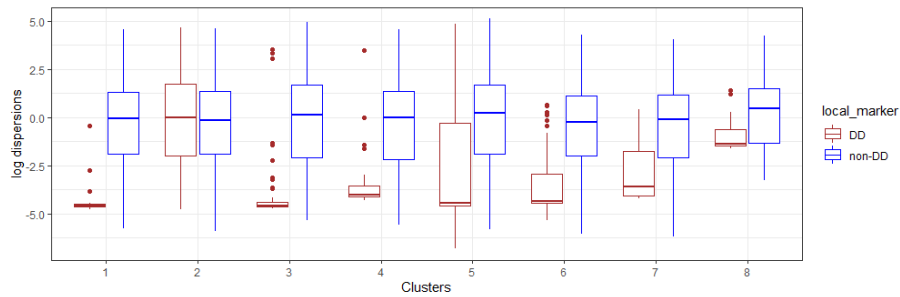
Web Figure C.36: Heat-maps to compare estimated unique parameters of local marker genes for each cluster. Columns in each heat map represent clusters and rows represent genes. The first two rows are the estimated mean expressions for the local DE genes and the last two rows are the estimated dispersions for the local DD genes. For all heat-maps, rows are reordered by local tail probabilities, hence genes on the top rows have a higher probability of being locally DE or DD.



Web Figure C.37: Posterior estimated relationships between the mean expressions and dispersions for each cluster. The posterior means of the mean expressions and dispersions are plotted. To compare the local marker genes for each cluster, we highlight local DE and DD genes in red, local DE and non-DD genes in green, and local DD and non-DE genes in blue.



Web Figure C.38: Distribution of posterior estimates of mean expressions for local DE and non-DE genes for each cluster.



Web Figure C.39: Distribution of posterior estimates of dispersions for local DD and non-DD genes for each cluster.

Web Table C.4: Top 10 local DE genes for each cluster.

Cluster 1	Cluster 2	Cluster 3	Cluster 4	Cluster 5	Cluster 6	Cluster 7	Cluster 8
Rgs16	Stmn2	Triobp	Neurog1	Raet1e	Jun	Neurog1	Xist
Ccng2	Ndn	Smpd3	Dctd	Cpne5	Nhlh1	Cntnap2	Hes1
Rasgef1b	Gap43	Satb2	Myt1l	Gucy1b1	Serpinb2	Dlk1	Eomes
Kif20a	Thra	Kcnk12	Lrrfip1	Lingo1	Nr2e1	Dcx	Cyr61
Ttk	Cnih2	Uncx	Ntng1	Unc5d	Fam107a	Lmo4	Cdo1
Melk	Gpm6a	Trp53inp1	Svop	Gm30146	Calb2	Hes1	Pdlim4
Cep55	Ina	Necab3	Fam107a	Prdm13	Sox1	Gpm6a	Rrm2
Sapcd2	Ly6h	Nr2f2	Isyna1	Srrm3	Ulk4	Meg3	Pcdhga6
C78859	Bhlhe22	Phyhipl	Dok5	Abca7	Elov17	Slc17a6	2310067P03Rik
Ptpre	Mapt	Sptbn2	Lpar1	Plvap	Tuba4a	Mbnl2	Gm5741

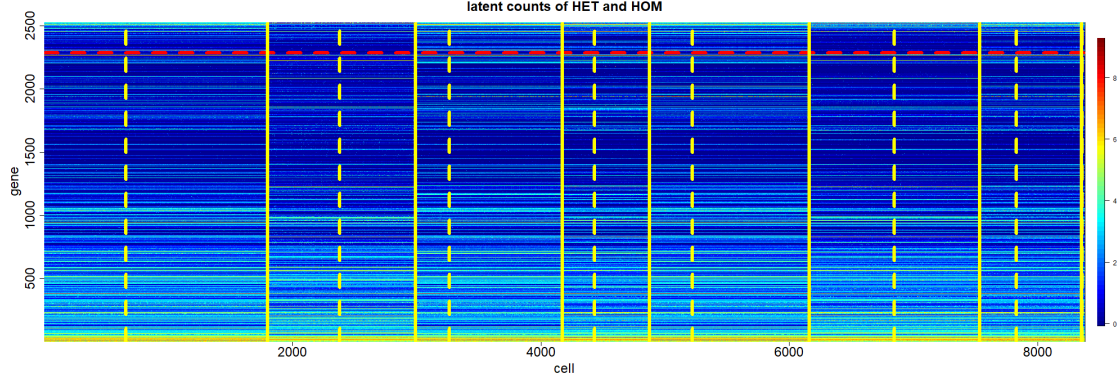
Web Table C.5: Top 10 local DD genes for each cluster.

Cluster 1	Cluster 2	Cluster 3	Cluster 4	Cluster 5	Cluster 6	Cluster 7	Cluster 8
Gm266	Dmrta2	Incenp	Dctd	Dut	Rspo3	Itm2b	Zfp935
Scg2	Pou3f3	Kif20a	Serping1	Esco2	Dmrta2	Neurod6	Pak1
Pabpc5	Tpbp	Cdca3	Olfml3	Paics	Nrarp	Perp	Qsox1
C78859	Emx2	Nr2f2	Trdn	Cdca7l	Lockd	Carf	Baiap2
Gm3693	Apoe	Phyhipl	Rnase4	Lingo1	Mlf1	Sorbs2	Them4
Creb3l1	Rtn1	Uncx	Ramp2	Dcaf17	Cks1b	Apobec2	Dlx6os1
Rasgef1c	Serpinh1	Sphkap	Nanog	Unc5d	Phgdh	Nid2	Xlra3a
Prdm13	Kcng1	Bcas1	Cpne5	Caln1	Foxj1	Rasgrf1	Gm5741
Gm17322	Tes	Gm48239	Prph	Pygm	Plvap	Hes1	Gm41231
Tbc1d30	Atp1a3	Kcnk12	Nr4a3	Bin1	Ppfia2	Celf5	Hist1h4d

C.5 Posterior Estimated Latent Counts

We compute the posterior estimated latent counts for all cells and compare between different clusters. Figure C.40 provides a heat-map of the estimated latent counts; cells are ordered by the clustering estimate, with solid vertical lines separating cells from different clusters and dashed vertical lines separating HET and HOM within cluster. Genes are reordered by global DD tail probabilities, with global DD genes above the horizontal line. Corresponding figures for the observed counts are shown in Web Section C.3.

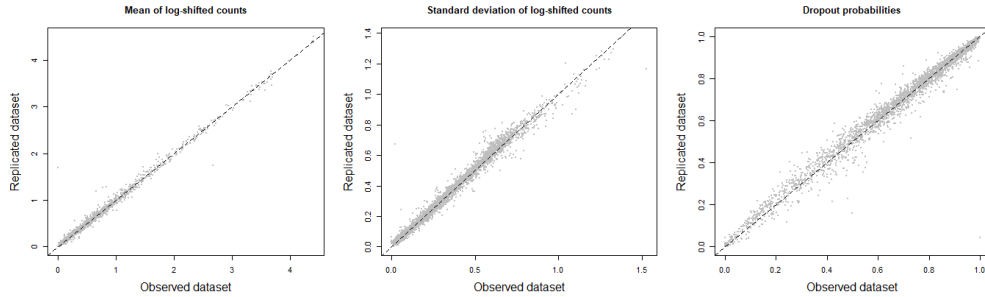
For each gene, posterior estimated latent counts and observed counts for cells within each clusters are similar, and clear differences are observed across cells from different clusters. In addition, we use t-SNE (a commonly used dimensional reduction method for visualising gene expressions) to visualize similarities between cells within each cluster and differences across clusters. Applying t-SNE to the posterior estimated latent counts for genes which are global DE and DD shows a clear separation between clusters.



Web Figure C.40: Heat-map of posterior estimated latent gene-counts for HET and HOM. Genes are reordered by global DE tail probabilities, genes above the red horizontal line are global DD, and vice versa. Cells for reordered by the point estimate of posterior allocations. Cells from different clusters are separated by solid lines and cells from different datasets are separated by dashed lines.

C.6 Posterior Predictive Checks

By comparing the observed and replicated statistics match gene-wise in Figure C.41, we show the observed and replicated statistics are similar which further supporting the model fit.



Web Figure C.41: Gene-wise comparison of the mean of the log shifted counts, standard deviation of the log shifted counts and dropout probabilities for posterior predictive checks with single replicate.

D Web Appendix D: Important Genes

We were provided with a list of 70 *important* genes, that are of particular interest for this experimental data. Information and summary statistics including the posterior estimated mean expressions and dispersions and global features of these *important* genes are shown below. As shown by these results, there are distinct patterns of the observed and posterior estimated latent counts for these genes across clusters. In addition, the under-represented cluster 2 seems to distinguish itself from all remaining clusters for the most *important* genes (in agreement with the results on local marker genes, i.e. cluster 2 has the greatest number of local markers).

In the following, we present the list of ‘important’ genes, along with a list of those which are classified as global marker genes in Web Table D.6, D.7 and D.8. In addition, we show the heatmap of the observed gene-counts and posterior estimated latent gene-counts for important genes only in Web Figure D.42 and D.43. Further, we present the relationship between posterior estimated mean expressions and dispersions with different local features in Web Figure D.44, D.45, D.46 and D.47. Lastly, we show the heatmap of estimated unique parameters for the important genes in Web Figure C.37.

Web Table D.6: List of important genes.

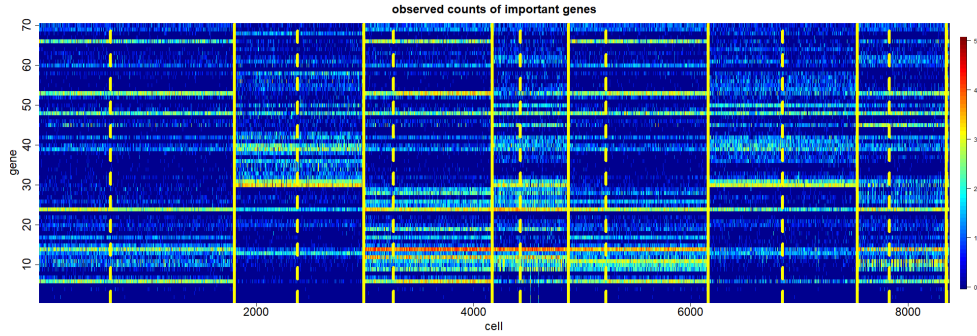
Dlx6os1	Sp9	Nrxn3	Dlx1	Ccnd2	Arx	Dlx5	Top2a	Rrm2	Pclaf
Hmgb2	Cdca7	Gm13889	Etv1	Cenpf	Gm26917	Sp8	Gad2	Hmgn2	Cenpe
Insm1	Nusap1	Tpx2	Neurod6	Cntn2	Mef2c	Mapt	Tbr1	Nrp1	Wnt7b
Id2	Neurod1	Nrxn1	Satb2	Neurog2	Crabp1	Lhx2	Zic1	Mfap4	Nrp2
Ccnd2	Nhlh1	Plcb1	Nhlh2	Lhx9	Lmo4	Prdm13	Emx2	Cited2	Insm1
Ptn	Cux2	Wnt7b	Pou3f3	Cux1	Pou3f1	Zbtb20	Nfix	Pfn2	Ube2c
Fezf2	Sox2	Neurod2	Sox5	Slain1	Fgfr1	Pou3f2	Robo2	Dlx2	Smc2

Web Table D.7: List of important genes which are classified as DE.

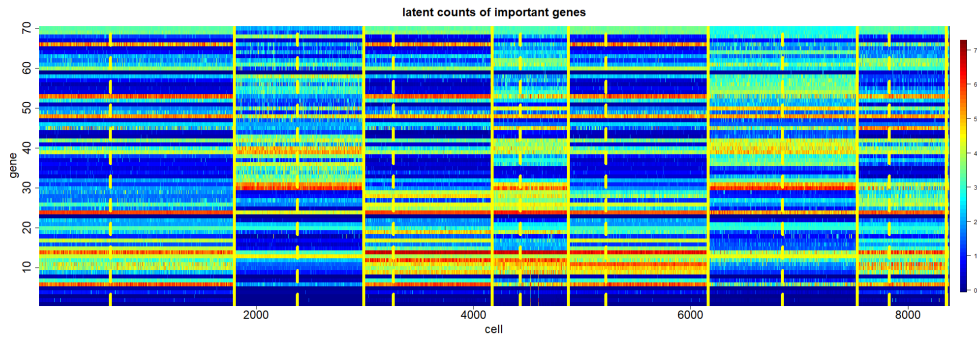
Dlx6os1	Nrxn3	Dlx1	Ccnd2	Arx	Dlx5	Top2a	Rrm2	Pclaf	Dlx2
Ube2c	Hmgb2	Cdca7	Gm13889	Cenpf	Sp8	Cenpe	Smc2	Nusap1	Sox2
Tpx2	Neurod6	Mef2c	Mapt	Tbr1	Nrp1	Wnt7b	Cntn2	Neurod2	Nrxn1
Neurod1	Satb2	Neurog2	Mfap4	Nrp2	Ccnd2	Nhlh1	Plcb1	Nhlh2	Crabp1
Lhx9									

Web Table D.8: List of important genes which are classified as DD.

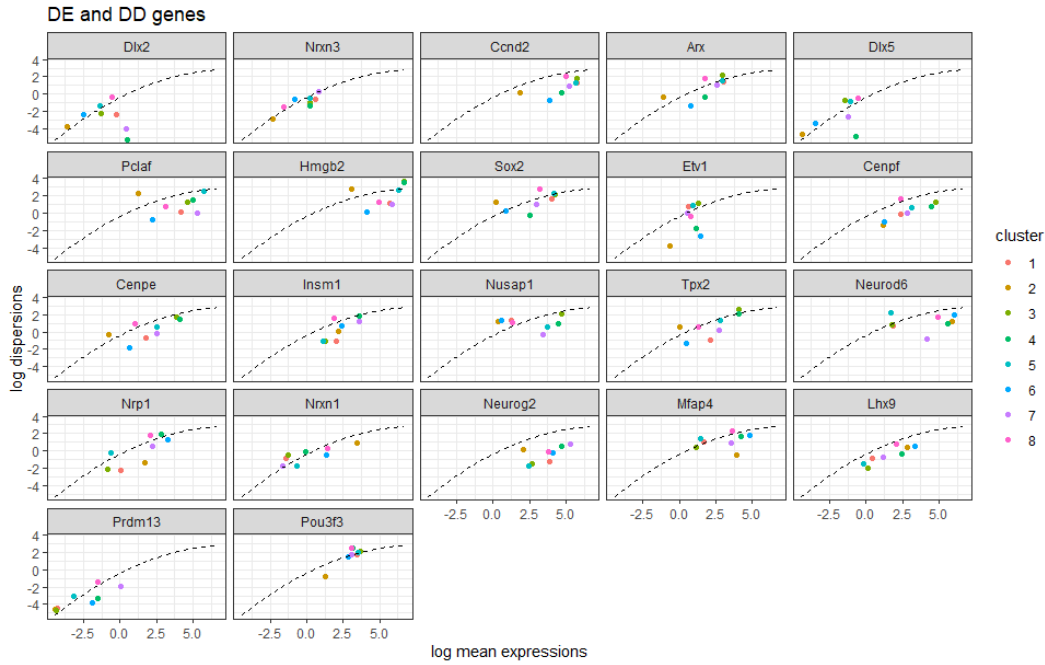
Arx	Dlx5	Pclaf	Hmgb2	Etv1	Cenpe	Insm1	Tpx2	Neurod6	Nrp1
Emx2	Insm1	Pou3f3							



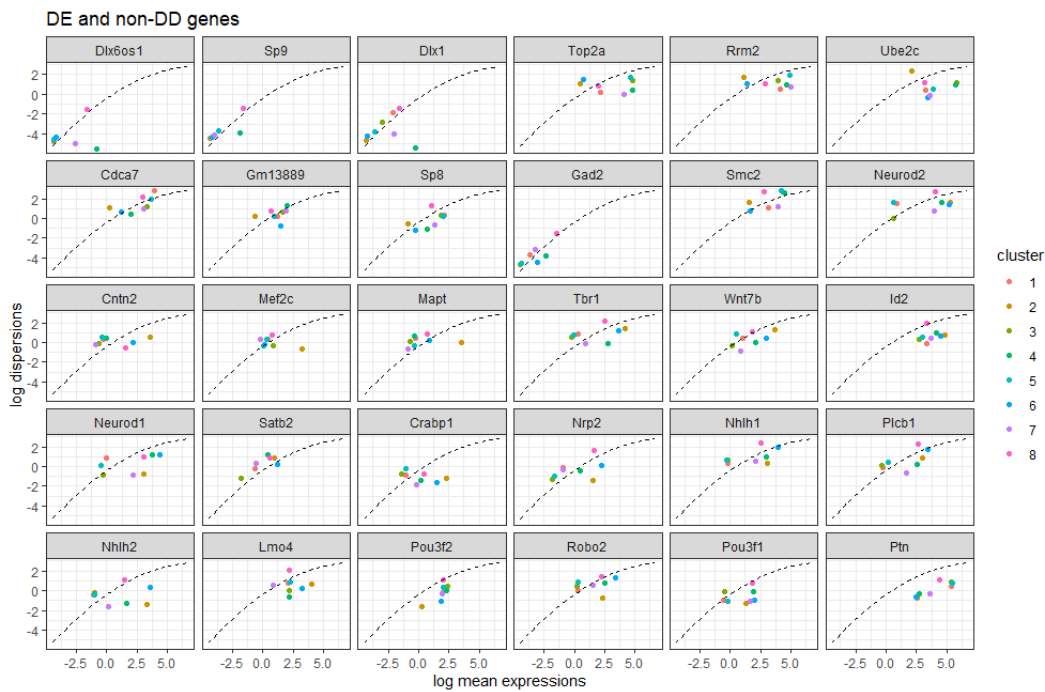
Web Figure D.42: Heatmap of the observed counts of important genes. Columns represent cells and rows represent genes. Cells are reordered by the estimated clustering. Cells from different clusters are separated by solid yellow vertical lines, and within each cluster, cells from HET and HOM are separated by dashed vertical lines.



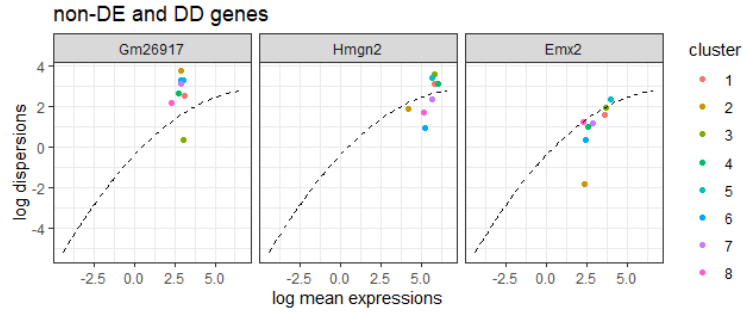
Web Figure D.43: Heatmap of the estimated latent counts of important genes. Columns represent cells and rows represent genes. Cells are reordered by the estimated clustering. Cells from different clusters are separated by solid yellow vertical lines, and within each cluster, cells from HET and HOM are separated by dashed vertical lines.



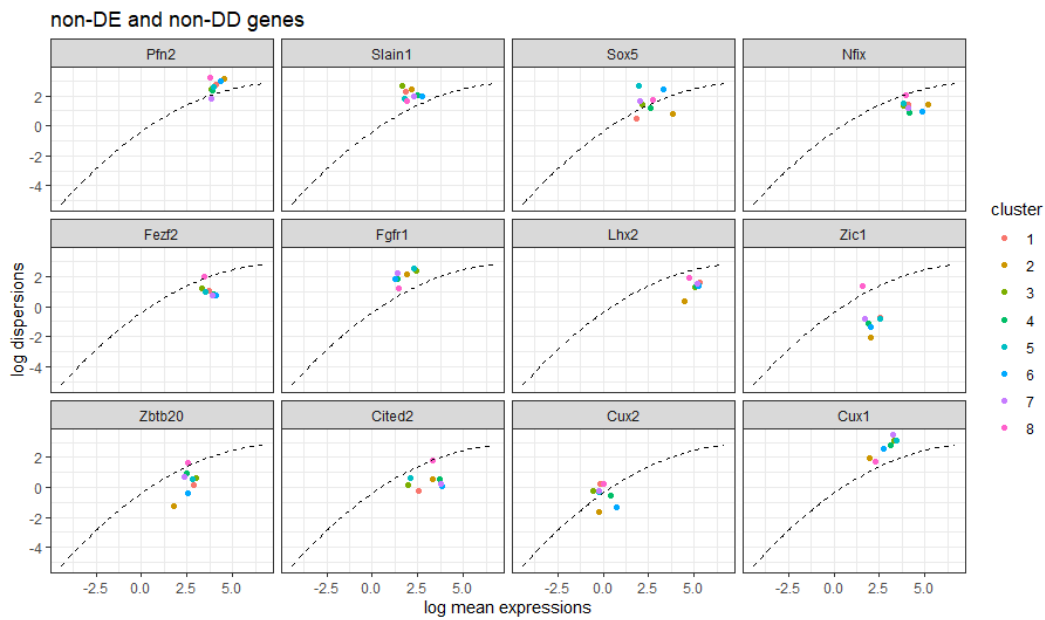
Web Figure D.44: Posterior estimated mean expressions and dispersions (on the log-scale) for the important genes which are classified as both DE and DD. The dashed line shows the posterior estimated relationship between the mean expressions and dispersions.



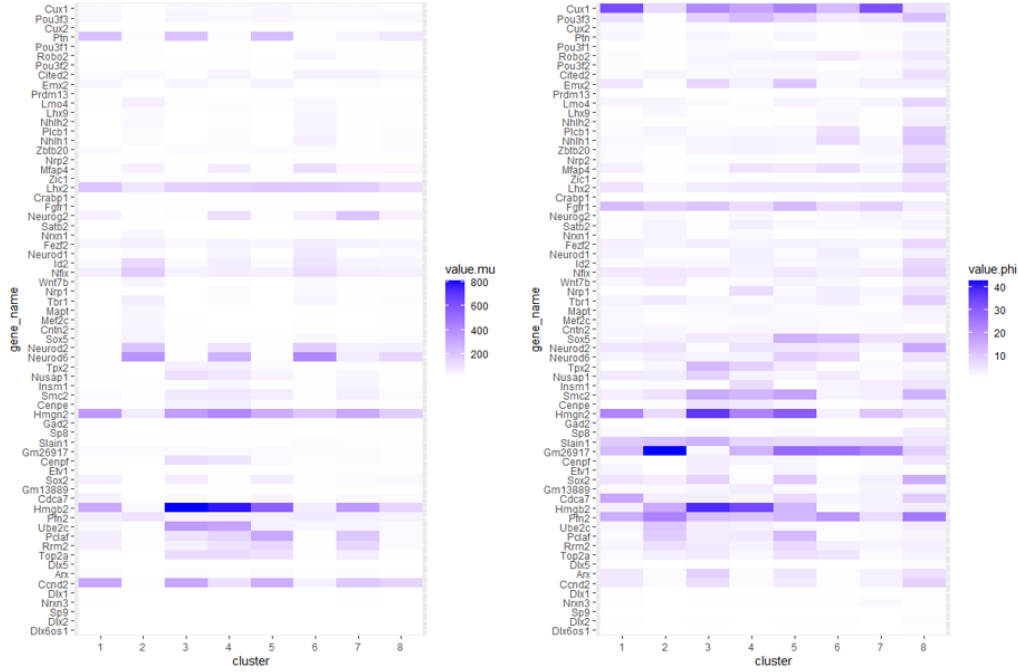
Web Figure D.45: Posterior estimated mean expressions and dispersions (on the log-scale) for the important genes which are classified as DE, but not DD. The dashed line shows the posterior estimated relationship between the mean expressions and dispersions.



Web Figure D.46: Posterior estimated mean expressions and dispersions (on the log-scale) for the important genes which are classified as DD, but not DE. The dashed line shows the posterior estimated relationship between the mean expressions and dispersions.



Web Figure D.47: Posterior estimated mean expressions and dispersions (on the log-scale) for the important genes which are classified as both not DE and DD. The dashed line shows the posterior estimated relationship between the mean expressions and dispersions.



Web Figure D.48: Posterior means of the unique parameters of important genes for all clusters for mean expression (left) and dispersion (right).

E Web Appendix E: Discussion

In this article, we have constructed an integrated Bayesian model for simultaneous normalization, imputation, and clustering of multiple single-cell RNA-sequencing datasets across different conditions. In this high-dimensional setting, our hierarchical Bayesian framework allows borrowing of information across conditions as well as measures of uncertainty in the estimated clustering. On simulated datasets, our proposed Norm-HDP model is robust and able to recover the true parameters and clustering, as well detect correctly the marker genes.

On the experimental dataset, the model estimates a total of eight clusters, which are all shared in the control and mutant conditions (with some uncertainty on further splitting some clusters). Certain clusters are under or over represented in the mutant condition when PAX6 is knocked out; this is further supported by the posterior of α , which is concentrated on small to moderate values, suggesting differences in cell-subtype proportions across the control and mutant conditions. Most *important* genes that were suspected to show differences across clusters and conditions are identified as marker genes, and additional marker genes have been detected (to be further investigated in future work). We note that tamoxifen administration was carried out at day E9.5, with embryos sacrificed and dissected at day E13.5. Future work will validate and explore additional data collected at day E14.5, which is anticipated to have stronger differences across conditions, potentially with unique gene expression patterns only present when PAX6 is knocked out.

For posterior inference, we have developed a Gibbs sampling algorithm, which produces asymptotically exact posterior samples. However, such algorithms may require a larger number of iterations to reach convergence and for a sufficiently large effective sample size. This can be particularly slow for scRNA-seq data, where the number of cells and genes are typically in the thousands. In future, we will develop a variational Bayes approximation [Hughes et al., 2015], requiring much fewer iterations. By comparing with the Gibbs sampling algorithm, we can investigate the tradeoffs in computation cost and approximation.

Although we focus on the HDP, the model could be extended to hierarchical processes based on priors beyond the DP, such as the hierarchical Pitman-Yor process [Teh, 2006] or more generally hierarchical normalized random measures [Camerlenghi et al., 2019]. An investigation and comparison of the induced prior distribution over the clustering structure and number of clusters, both within and between datasets, is provided in Argiento et al. [2020]. Moreover, the MCMC algorithm developed here can be extended based on finite-dimensions approximations of normalized random measures [Lee et al., 2016]. Other potential model extensions include cluster-specific mean-dispersion relationships for increased flexibility.

References

- R. Argiento, A. Cremaschi, and M. Vannucci. Hierarchical normalized completely random measures to cluster grouped data. *Journal of the American Statistical Association*, 115(529):318–333, 2020.
- F. Camerlenghi, A. Lijoi, P. Orbanz, and I. Prünster. Distribution theory for hierarchical processes. *Annals of Statistics*, 47(1):67–92, 2019.
- J.E. Griffin and D.A. Stephens. Advances in Markov chain Monte Carlo. In *Bayesian Theory and Applications*, pages 104–144. Oxford University Press Oxford, 2013.
- M. Hughes, D.I. Kim, and E. Sudderth. Reliable and scalable variational inference for the hierarchical Dirichlet process. In *Artificial Intelligence and Statistics*, pages 370–378. PMLR, 2015.
- J. Lee, L.F. James, and S. Choi. Finite-dimensional BFRY priors and variational Bayesian inference for power law models. In *Proceedings of the 30th International Conference on Neural Information Processing Systems*, pages 3170–3178, 2016.
- Y.W. Teh. A hierarchical Bayesian language model based on Pitman-Yor processes. In *Proceedings of the 21st International Conference on Computational Linguistics and 44th Annual Meeting of the Association for Computational Linguistics*, pages 985–992, 2006.
- C.A. Vallejos, S. Richardson, and J.C. Marioni. Beyond comparisons of means: understanding changes in gene expression at the single-cell level. *Genome Biology*, 17(1):70, 2016.